Title

Mass-modulation schemes for a class of wave energy converters: Experiments, models, and efficacy

Authors

Diamond, Christopher A
Judge, Carolyn Q
Orazov, Bayram
et al.

Publication Date

2015-08-01

DOI

10.1016/j.oceaneng.2015.05.018

Peer reviewed

Mass-modulation schemes for a class of wave energy converters: Experiments, models, and efficacy

Christopher A. Diamond[a], Carolyn Q. Judge[b,*], Bayram Orazov[a], Ömer Savaş[a], Oliver M. O'Reilly[a]

[a] *Department of Mechanical Engineering, University of California at Berkeley, Berkeley CA 94720, USA*

[b] *Naval Architecture and Ocean Engineering, United States Naval Academy, Annapolis, MD 21402, USA*

Abstract

In a recent series of works, mass-modulation schemes have been proposed for a class of ocean wave energy converter (WEC). The goal of the schemes is to improve the energy harvesting capabilities of these devices by taking advantage of the ambient water. However this improvement comes at the cost of increased system complexity and possible impulse loadings at the instances where the mass changes. In the present work, experimental results for a pair of these schemes are presented and one of them is shown to be effective in increasing the energy harvesting potential of a WEC. Building and testing prototype WECs is costly and challenging and so, in order to examine as wide a range of parameters and designs as possible, a detailed two degree-of-freedom model is developed for a WEC equipped with a mass-modulation scheme. Numerical analysis of the model also shows the potential benefits of the mass-modulation scheme.

Keywords: Ocean Wave Energy Converter, Energy Harvesting, Piecewise-smooth Dynamical Systems

1. Introduction

A subset of ocean wave energy converters (WEC) feature heaving buoys, utilizing methods of energy extraction originally proposed in the mid 1970s (Evans, 1976, 1982; Mei, 1976; Salter, 1974). These methods form the basis of much current research in the area of ocean wave energy harvesting where part of the power of the incident waves is converted to electrical power. As with many other energy harvesting devices that exploit resonance, these devices have a relatively narrow bandwidth (Stephen, 2006; Tang and Zuo, 2011). Consequently, accurately predicting and, if possible, actively modifying the resonant behavior in response to changes in the frequency of the incident waves is critical. Similar to energy harvesting devices in other application areas (see, e.g., the recent review by Daqaq et al. (2014)), any improvement in the response in the neighborhood of a resonance relative to an unmodified harvester will improve the appeal

*Corresponding author, judge@usna.gov

of the device. As a result, central issues in the type of WEC of interest in this paper are modeling the dynamics of these devices (e.g., Falcão et al. (2012)) and the development of control strategies which either actively tune a resonant frequency of these devices to the frequency of the dominant incident waves (as in Dick (2005)) or latches the motion of the WEC to that of the incident waves (as in Babarit et al. (2004); Falnes (2002)).

To improve the energy extraction capabilities of a buoy WEC that exploits resonance phenomena, we have taken an approach different than the aforementioned schemes (which either alter a resonant frequency or involve latching control). Instead, we have proposed a scheme to vary the effective mass of the device within each wave cycle (see Figure A.1). This modulation can be achieved by either trapping water and/or varying the hydrodynamic added mass of the WEC in a manner that produces a state-dependent switching of the mass parameter. The goal of this variation is to increase the velocity of the relative heaving motion of the system thereby improving energy harvesting. Part of the inspiration for the method came from the response amplification observed in the resonant behavior of parametrically excited systems (see, e.g., Rhoads et al. (2008); Rugar and Grütter (1991); Wirkus et al. (1998)).

In our earlier works, we proposed a heaving buoy WEC design that was distinguished from contemporary WECs (see, e.g., Goggins and Finnegan (2014); McCabe (2013); Vicente and Justino (2013); Yeung et al. (2011); Zurkinden et al. (2014)) by the aforementioned mass-modulation scheme. This WEC design was analyzed in Orazov et al. (2010, 2012) and an experimental prototype tested in Orazov (2011). The analysis of Orazov et al. (2010, 2012) demonstrated that significant improvement in energy harvesting could be achieved using the innovative mass-modulation scheme. Furthermore, in Orazov (2011), it was found that improvements in the energy harvested could be achieved, but significant momentum losses which were neither anticipated nor modeled in Orazov et al. (2010, 2012) were also observed. These losses were determined to be associated with momentum conservation at several discrete stages of the mass modulation. The observed momentum loss necessitated exploration of alternative mass-modulation schemes and the development of a new set of models.

The purpose of the present paper is to extend our earlier work (Diamond et al., 2013) where new sets of mass-modulation schemes were presented, and a simple one degree-of-freedom model was used to explore their efficacy. In the present paper, experimental results for the optimal mass-modulation scheme, known as Scheme III, proposed in Diamond et al. (2013) are presented. These experiments verify a potential improvement in energy harvesting. However, the testing facility and prototype WEC allow only limited adjustment of key design and environmental parameters. As these parameters affect the optimality of any one given mass-modulation scheme, an enhanced model was sought which could be used to determine the system's sensitivity to a wider range of parameters. The resulting two-degree-of-freedom model accounts for the momentum loss and incorporates a more realistic representation of hydrodynamic interactions. The main insight this model provides is to show that the mass modulation Scheme III will work for a wide variety of parameter choices. Particularly important is a parameter related to momentum loss: designing a WEC where the momentum loss associated with the mass-modulation scheme is minimized is shown to be key.

An outline of the paper is as follows. First, we present a broader discussion of the mass-modulation schemes. Next, we give a brief overview of the experiments on a system similar to the first model described in Orazov et al. (2010) in Section 3.1 and show how

they motivated the creation of the second model described in Diamond et al. (2013) and exploration of new mass-modulation schemes. One such scheme, which we refer to as Scheme III, was considered to be optimal for the one degree-of-freedom model used in Diamond et al. (2013). In Section 3.2, results from a series of experiments on a prototype WEC equipped with a power-take-off element (PTO) are presented. Next, in Section 4, we establish the two-degree-of-freedom model for the WEC prototype which accommodates hydrodynamic effects that were absent in our earlier single degree-of-freedom models. To facilitate using this model to explore parameter regimes for a mass-modulated WEC, an energy harvesting metric is defined in Section 5. We discuss the effect on our metric of varying individual parameters in Section 6 and present our conclusions in Section 7.

2. Mass-Modulation Schemes

Heaving buoy ocean wave energy converters (WECs) harvest energy by exploiting the oscillation of the buoy in response to incident waves. In order to optimize its energy harvesting capabilities, the WEC is designed so that one of its resonant frequencies is close to the dominant frequency of the incident waves. Designing and operating a buoy WEC is challenging. Among the many challenges, WECs operate in a harsh environment where maintenance can be difficult and the necessary design and wave tank testing of scaled prototypes is expensive and time consuming. Clearly, any scheme that can effectively improve the energy harvesting of a WEC is worth examining.

One scheme that we believe can improve the energy harvesting capabilities of a WEC is a mass-modulation scheme. In such a scheme, the mass of an element of a WEC is varied in time. This variation can take several forms. One option is to actively change the geometry of one of the floats of the WEC and thereby change its hydrodynamic added mass. Another option is to periodically enclose and later release a volume of water in one of the floats. Such modulation takes advantage of the fluid environment and incident waves and can be viewed as a form of parametric excitation. The latter is a well-known phenomenon that has been used to amplify the response of oscillating systems (Rugar and Grütter, 1991), in such varied settings as MEMS oscillators and oscillating water columns (Olvera et al., 2007; Rhoads et al., 2008).

The first such mass-modulation scheme was examined in Orazov et al. (2010) and was further investigated and improved in Diamond et al. (2013) and Orazov et al. (2012). Referring to Figure A.1, in the present context of WECs, the mass of the inner float of a buoy WEC is modulated in time. If the inner float is completely submerged as shown in the figure, then the mass-modulation can be entirely attributed to the change in the hydrodynamic added mass of the inner float as the flaps are opened and closed.

There are no theoretical restrictions on the frequency and duration of mass modulation that may be specified. Indeed, there exist infinitely many mass-modulation schemes that can be concocted. Generally, parametric excitation is most successful when it occurs at around twice the fundamental, or natural, frequency of an oscillator. The naval architecture of a heaving buoy WEC is such that its fundamental frequency is in the neighborhood of the commonly encountered incident wave frequency. Thus, guided by the literature (Olvera et al., 2007; Rhoads et al., 2008; Rugar and Grütter, 1991) on parametric excitation, the initial work on these schemes in Orazov et al. (2010, 2012) focused on modulation at approximately twice the frequency of wave forcing.

While it is possible to conceive of a control system which would use the fluid surrounding the WEC to modulate the mass in any conceivable manner, our focus has been on the development and implementation of mass-modulation schemes that can be realized passively. In our early designs, we found that passive mass modulation could be implemented by alternatively allowing water flow, through some section of the WEC, and blocking water flow through that same section. When the flow is blocked, a pressure associated with the impeded flow and the inertial force of moving the newly trapped volume of water are created, relative to the case where the flow was unimpeded. For a given velocity, these effects are assumed to be proportional only to the acceleration of the mass, and as such they may be grouped with a mass term. This results in an increase in effective mass - a mass modulation.

Three such schemes are shown in Figure A.2. The schemes feature modulation by a fraction μ of the mass M_1^{Off} of an inner float M_1 when the mass is not being modulated and the variables x_1 and $\dot{x}_1$ denote the respective (heaving or vertical) displacement and velocity of M_1. Thus the mass of M_1 changes from

$$M_1^{\text{On}} = M_1^{\text{Off}} + \mu M_1^{\text{Off}} \tag{1}$$

to M_1^{Off}. It is critical to note here that the mass modulation μM_1^{Off} is dependent on the state of the system and so the models for the WEC will feature state switching and possibly impulsive loading when the mass of M_1 changes from M_1^{Off} changes to M_1^{On} and vice versa.

For example, Figure A.3 illustrates two possible implementations of the mass-modulation scheme shown in Figure A.2(c). The masses in this figure are connected by a power-take-off system which is not shown and both heave in response to the incident waves. The mass M_1 is equipped with a mechanism that enables it change its effective mass by an amount μM_1^{Off}. The realization shown in Figure A.3(i) only involves changes to the hydrodynamic added mass while the design shown in Figure A.3(ii) involves changes both to the hydrodynamic added mass of M_1 and an additional change in M_1 due to the enclosed mass of water:

(i) For the realization shown in Figure A.3(i), μM_1^{Off} is equal to the difference in the hydrodynamic added mass of M_1 when the flaps are in the open state compared to the closed state.

(ii) For the realization shown in Figure A.3(ii), μM_1^{Off} is equal to the change in hydrodynamic added mass of M_1 plus the effect of the enclosed mass.

The modulation scheme is accompanied by an impulsive loading on the mass M_1 which alters the dynamics of the WEC and this may have a detrimental effect on the harvesting capabilities. Experimental results for Schemes I & III will be discussed in Section 3. We also emphasize that the realization emphasized in this paper is the one shown in Figure A.3(i).

It is not immediately apparent that a mass-modulation scheme should be effective in improving the energy harvesting capabilities of a WEC. Such schemes are difficult to faithfully model, are hindered in effectiveness by the increased damping and impulsive loading introduced by the mass-modulation mechanism, and are difficult to implement in a prototype. Part of the purpose of the present paper is to show how Scheme III above overcomes many of the technical challenges of the earlier Schemes I and II and

successfully yields improvements to energy harvesting. We illuminate this improvement with the help of a model that is far more realistic than the ones used in our earlier works (Diamond et al., 2013; Orazov, 2011; Orazov et al., 2010, 2012) and by experimental testing of a prototype.

3. Experimental Results

While it is straightforward to propose a mass-modulation scheme, significant challenges arise when attempting to implement a scheme in a prototype. The first scheme for which a prototype was designed and tested was Scheme I and the results of this testing are recorded in Orazov's dissertation (Orazov, 2011). We report these results below in Section 3.1 because, among others, they serve to illuminate features of the mass modulation that weren't considered in our earlier models. These results also bear contrast to those for Scheme III which we report in Section 3.2.

3.1. Experimental Results: Scheme I

Initial experimental work involved the construction of a small scale prototype WEC to verify the previously proposed (Orazov et al., 2010, 2012) mass-modulation Scheme II at the UC Berkeley Tow Tank facility in Richmond, CA (Figure A.4). This facility employed a hydraulically actuated and electronically controlled vertical-flap wave maker to independently set incident wave frequency and amplitude.

As can be seen in Figure A.5, a scale prototype of the WEC was constructed of three parts: an outer float and guides, an inner float which was concentric to the outer float, and the water entrapment mechanism, which is rigidly attached to the inner float. Two deviations were made from the earliest model in Orazov et al. (2010, 2012) and this experiment: no power-take-off system, or power-take-off modeling damper, was implemented, and a spring loaded latching mechanism that was to initiate the twice-per-period mass modulation was simplified to a once-per-period mass modulation due to difficulties in realizing the switching in the experimental setup. In terms of Figure A.2, Scheme I was tested instead of Scheme II.

Figure A.6 shows two phase portraits, one simulation generated using a one degree-of-freedom model in (a) and one physically realized (from this experiment) in (b). In both we can observe a downward jump in velocity when the upper flaps close and mass is effectively added, and it is notable that good agreement is seen between the modified theory and the experiment generally. We invite the reader to contrast this jump in velocity with the corresponding portrait shown in Figure A.7 where no flaps are installed and the mass is unmodulated: no velocity jump is observed when the flaps are absent. This is a consequence of the conservation of momentum, which at the time of the experiments reported in Orazov (2011) was not accounted for in the one degree-of-freedom model. The jump's appearance in Figure A.6 provoked a reassessment of the original theory and the creation of an updated single mass model discussed in (Diamond et al., 2013, Eqns. (1)–(4)). This updated model was used here to generate Figure A.6(a), which is in good agreement with the measurements shown in Figure A.6(b).

Agreement between experimental results and theory, as modified by momentum considerations in Diamond et al. (2013), was encouraging, but several questions provoked by the experiment needed to be addressed. Power-proportional damping was absent in

the experimental setup. Lack of this damping has the potential to alter the dynamics from those specified by the model. Moreover, updated boundary conditions implemented in light of momentum considerations mentioned above were incorporated into Diamond et al. (2013). These conditions corresponded to Scheme III, and this scheme warranted its own investigation.

3.2. Experimental Results: Scheme III

Improved experimental realization of the mass-modulated WEC required the addition of a power-proportional damper. To model the damping provided by a PTO, a stepper motor, rotated by the relative motion between the inner and outer floats via a rack-and-pinion mechanism, was installed on the prototype. A discussion of this type of power generator and its applicability to our model follows in Section 3.2.1. Additionally, testing of Scheme III necessitated a new mechanism to modulate the mass. A simple, passive mechanism was designed which is briefly presented in Section 3.2.2.

3.2.1. The Power-Take-Off Element

A simple PTO is constructed by placing a resistive load $\mathcal{R}_L$ between two leads of a properly configured common stepper motor. The rack-and-pinion mechanism translate the relative heaving motion into a rotary motion at the shaft of the stepper motor, thus generating power. Determination of the damping applied between the inner and outer floats at a given relative velocity is dependent on the effective moment arm of the pinion gear (r_P) and the torque τ_M generated by the motor at a given rotational speed ($\tau_M = \tau_M\left(\dot{\theta}; \mathcal{R}_L\right)$). As the torque $\tau_M = \tau_M(\dot{\theta}; \mathcal{R}_L)$ is generally not an analytic function, it was experimentally determined for a variety of resistive loads $\mathcal{R}_L$ and rotational speeds $\dot{\theta}$. Two motors - a Slo-Syn M062-FC-404B and a Slo-Syn M092-FD-416E - were characterized by measuring the power applied to a third motor to rotate them at a known speed with a known resistive load. A sample of the characterization data may be seen in Figure A.8.

It is instructive to recall here from the literature on single degree-of-freedom mass-spring-damper oscillators of the form $m\ddot{u} + (b_e + c)\,\dot{u} + ku = A\cos(\omega t)$ that are equipped with a PTO modeled as $b_e\dot{u}$ that optimal harvesting is achieved when $\omega^2 = \frac{k}{m}$ and $b_e = c$ (see, e.g., Salter (1974); Stephen (2006)). While the corresponding optimal conditions are not known for the models employed in this paper, these results for the simpler model serve as useful benchmarks. Referring to Figure A.8, it is readily apparent that the damping provided by the stepper motor PTO is quite different than the linear proportional damping that is typically considered in models for PTOs (Salter, 1974; Stephen, 2006). In the latter works, the power P extracted by the PTO is assumed proportional to the relative velocity v_{rel} between the heaving bodies:

$$\mathrm{P} = \mathbf{F}_{\text{PTO}} \cdot \mathbf{v}_{\text{rel}} \approx c_{\text{PTO}} v_{\text{rel}}^2 \tag{2}$$

where c_{PTO} is a positive constant. Similiarily in our models, the damping force is assumed to be positively proportional to the relative velocity between the floats, through the pinion gear of moment arm r_p. For the sake of our models' fidelity, we would desire $\mathrm{P} \sim c_{\text{PTO}} r_p^2 \dot{\theta}^2$. As can be seen from Figure A.8, however, the damping torque is negatively proportional to the speed of the relative velocity between the floats, where this

proportionality is given by κ_τ, with a non-zero holding torque (a torque up to which the motor can resist turning) τ_H. Moreover, the proportionality constant changes depending on the operational velocity regime and load resistance: $\kappa_\tau = \kappa_\tau\left(\dot{\theta}; \mathcal{R}_L\right)$, and the holding torque additionally depends on the load resistance, or $\tau_H = \tau_H\left(\mathcal{R}_L\right)$. Thus power extracted by the PTO is given by

$$\mathrm{P} = \tau_M(\dot{\theta}; \mathcal{R}_L) \cdot \dot{\theta} = \tau_H\left(\mathcal{R}_L\right) \cdot \dot{\theta} - \kappa_\tau\left(\dot{\theta}; \mathcal{R}_L\right) \cdot \dot{\theta}^2. \tag{3}$$

As such, the optimal damping for single degree-of-freedom oscillators mentioned above could not be exactly recreated here. Regardless, this new PTO was used, as it would affect the mass modulated and unmodulated versions of the prototype identically and would be far more representative of a real system than that considered in the previous experimental work. Additionally, we now take this opportunity to note a few methods of enhancing this PTO.

If we restrict our attention to the area of low rotational speeds, or roughly less than ten radians/second, we notice that the holding torque τ_H decreases, and the magnitude of the torque/rotational speed proportionality increases, with increasing $\mathcal{R}_L$. For a direct rack-and-pinion setup - one absent adjustable gearing - r_p may easily be selected for these sort of rotational speeds. This suggests that, if desired, there is the potential that the resistive load $\mathcal{R}_L$ could be adjusted via a control scheme, on some larger timescale, to achieve a desired effective damping. If a variable gearing and clutch setup were incorporated to interface the relative motion of the masses to the PTO, r_p could be a function of various parameters and even more general control schemes could be constructed to tune the optimal damping in real time.

Additional study of the new type of damping, and determination of its optimal value, may reveal a great deal about the desired PTO method for a mass modulated WEC, but such an investigation is beyond the scope of the work presented here. In the end, only the smaller M062-FC-404B was used, as it was experimentally determined that the larger M092-FD-416E provided excessive damping for the prototype, effectively attenuating almost all relative motion.

3.2.2. Scheme III Mass-Modulation Mechanism

Updated optimal mass modulation boundary conditions in Diamond et al. (2013) necessitated a new mechanism and a passive, flap-based mechanism was desired for ease of construction. In such a case Scheme III requires closing of the flaps, resulting in the onset of the modulated-mass regime, at the points of zero velocity of the inner float, and the opening of the flaps, resulting in onset of the unaltered mass regime, at the points of maximum absolute velocity. These latter points coincide in time with those where the maximum pressure is exerted by the surrounding fluid on the flaps if they are in the closed position. We hypothesized that we could set the force resisting this pressure by the flaps - for the maximum inner float velocities encountered in the previous experiments - to be just defeated at these points of maximum velocity, closely approximating the mass modulation we desired.

One set of flaps was able to provide the mass modulation in both directions, as opposed to the two sets required previously for Scheme II which had caused significant problems. The remaining pair of flaps were made of newly fabricated acrylic semicircles,

identical in thickness to those considered previously for Scheme I, cut about 0.75 cm shorter in radius than before. Large rubber semicircles were affixed to these flaps and, by observationally verified trial and error, were cut down to the size corresponding to flap opening due to fluid pressure at the moment of max velocity (approximately 191mm long 85mm wide). Similar to (Orazov, 2011), this method of resisting fluid pressure, and thus affecting added mass, was not remotely adjustable and was still dependent on the characteristics of the incident wave, but it was much closer to the optimal mass-modulation Scheme III discussed in Diamond et al. (2013). The same mechanism could be made, in a more advanced prototype, to be remotely adjustable through a variety of methods, but such was not necessary for the scope of our experiments.

3.2.3. Experimental Testing and Results

Apart from the aforementioned changes to the prototype, a few changes to the experimental procedure used in Orazov (2011) and discussed previously in Section 3.1 were also made. First, power collected by the PTO was monitored in real time by an oscilloscope placed in parallel to one of the resistors between the leads of the PTO. Secondly, the prototype was moored by three lines to the sides of the tow tank, rather than the test platform (or carriage), as previously. Thirdly, the range of excitation frequencies was changed from 0.60 Hz $\leq f \leq$ 0.76 Hz to 0.65 Hz $\leq f \leq$ 0.85 Hz: the addition of the PTO was determined to have made the response of the prototype more regular to a larger range of frequencies, and reduced the relative motion at frequencies below 0.65 Hz. Additionally, the excitation wave amplitude was increased from 10 ± 1 cm to approximately 15 ± 1.5 cm for all excitation frequencies for the same reason. Beyond these changes, the experimental setup, experimental procedure, and data collection methods are as they were in Orazov (2011), and we refer readers to this dissertation for more detailed information.

A comparison of important system responses, for the modified prototype both with and without mass modulation, for six selected incident wave forcing frequencies is presented in Table A.1. For ease of comparison, we have also attached a table of system responses from the initial testing in Table A.2. Additionally, we note that mean values are computed in the root-mean-square (RMS) sense, i.e.

$$f(t)^{\mathrm{RMS}} = \sqrt{\frac{1}{T_f - T_0} \int_{T_0}^{T_f} f(\tau)^2 \, d\tau}$$

Firstly, and perhaps most important, we can see the effect of changing the mass-modulation regime; at no testing frequency in the current experiment was the RMS relative velocity with mass modulation found to be less than that without mass modulation. Under the previous regime, this was not the case: notice that when the forcing frequency was more than 0.2 Hz away from the estimated fundamental frequency $f_0 = 0.66$ Hz of the WEC prototype, the RMS relative velocity is less in the mass modulated case. Notably, the RMS relative velocity without mass modulation only matched that with mass modulation at the forcing frequency of $f = 0.800$ Hz. It is likely that this frequency is close to a local minimum in the system's response $\Delta v^{\mathrm{RMS}}(f)$ between the fundamental frequency f_0 and some harmonic f_n.

Secondly, the RMS relative velocity with mass modulation is significantly larger than was the case without mass modulation at most frequencies, doubling the case without

mass modulation at $f = 0.650$, 0.675, and 0.750 Hz. Examining the RMS inner mass velocity at the various testing frequencies reveals that, in most of the cases, the values with mass modulation are lower than those without, so we suspected that the mass modulation was affecting a greater average phase lag of the velocity of the inner mass relative to the outer float, $\bar{\tau}$. These values were calculated and may be seen in Table A.3. It is evident that mass modulation results in a larger phase lag than that seen without mass modulation, so it can be deduced that this plays at least some part in overcoming the reduced RMS velocity of the inner float in the mass modulated case.

Finally, and also seen in Table A.3, we calculated the RMS power delivered by the PTO with the resistive load $\mathcal{R}_L = 4.6\ \Omega$ attached at both of the lead pairs. Again we can see that, excepting the forcing frequency $f = 0.800$ Hz (where the power is similar in both cases), the addition of mass modulation results in greater generated power. It cannot be emphasized enough that this result was for an effective damping fundamentally dissimilar from the viscous damping assumed in the theory, and for a curve of that dissimilar damping that was selected without much evidence as to its optimality. This points towards the robustness of mass modulation's effect on power harvesting. The frequency excepted from this trend may be explained by appealing to the RMS relative velocities in both cases: they are very close, and as such it is not at all surprising that the RMS power extracted might be slightly lower in the mass modulated case, as the process of producing an RMS mean in velocity would miss nonlinearities in the power generation that would matter to the RMS mean of power.

The above results point to validation of the incorporation of phase-dependent mass modulation on a buoy-type WEC or, more specifically, an effective modulation achieved by blocking the free-flow of water through some part of a WEC, twice a period, thus harnessing an added mass effect. Generally, these results also show that mass modulation is realizable on a buoy type WEC even in the (comparatively) unrefined prototype stage. In the authors' opinion, it was suspected that mass modulation would be realizable on a buoy type WEC of arbitrary geometry with appropriate alternating flow-through/flow-blocking areas.

There are still some questions as to the robustness of Scheme III mass-modulation. Our experimental work had taken place on a scaled-down prototype of (obviously) specific inner and outer float mass and geometry. How might the scheme perform if these parameters were drastically different? How might hydrodynamic damping of the masses and between the masses, particularly if taken as a function of forcing frequency, change the performance? How might the performance change over a free selection of added mass onset and removal in phase space? Generally, we desired the ability to perform some sort of a numerical sensitivity analysis on a more advanced system to a wide variety of design and environmental parameters which would be extremely difficult or impossible to change in an experimental setup. From such an analysis, we could extend the specific conclusion from the experiment - that mass modulation is beneficial to WEC power harvesting for a wide range of incident frequencies - from our specific prototype to a larger subset of WECs. Accordingly, we now examine a two-degree-of-freedom model subject to such a numerical analysis below.

4. Two Degree-of-Freedom Model for the Wave Energy Converter

To perform our numerical analysis, a new hybrid-dynamical model is necessitated. We model the heaving buoy WEC as a two-degree-of-freedom mass-spring-dashpot system. The mass M_2 models the upper floating body while M_1 models the submerged body (inner float) which is connected to M_2 by a PTO. A schematic of the oscillator is shown in Figure A.11 and is a more comprehensive model than the one analyzed in earlier works (Diamond et al., 2013; Orazov, 2011; Orazov et al., 2010, 2012; Rougirel, 2013). By way of background, the stiffnesses $k_{1,2,3}$ and viscous damping parameters $c_{1,2,3}$ in the model represent both mechanical and hydrodynamical forces on the masses. Here, $c_2 = c_2' + B$, where B is the damping contribution exclusively from the PTO. In a typical operating environment for the WEC, the six parameters $k_{1,2,3}$ and $c_{1,2,3}$ generally depend on the frequency ω of the incident forcing. As discussed in the forthcoming subsections, these parameters along with the mass M_1 may also depend on the mass modulation.

4.1. Mass-modulation

The unique feature of the model is that the mass M_1 of the inner float varies in a state-dependent manner. That is, if x_1 denotes the displacement of M_1, then the mass of M_1 depends on the value of the pair $(x_1, \dot{x}_1)$. The locations in the $x_1 - \dot{x}_1$ phase plane where the mass changes (cf. Figure A.12) are known as switching boundaries $\mathcal{S}$ and the conditions under which M_1 changes are known as switching conditions. Referring to Figure A.12, we follow Diamond et al. (2013) and define two angles α and β for the locations of the switching boundaries. More simply, referring to Figure A.12, it is convenient to define

$$\theta = \arctan\left(\frac{x_1}{\dot{x}_1}\right), \ 0 \leq \theta < 2\pi \tag{4}$$

so that

$$\theta \in \begin{cases} \mathfrak{T}_A & \text{if } \alpha < \theta < \alpha + \beta \text{ or } \alpha < \theta - \pi < \alpha + \beta \\ \mathfrak{T}_0 & \text{otherwise} \end{cases} \tag{5}$$

where $\mathfrak{T}_A$ and $\mathfrak{T}_0$ are the sets of all θ in the mass-modulated and rest mass regimes, respectively. Then, between angle α in the phase plane (defined off of the positive $\dot{x}_1$-axis) and angle β (defined off of the ray created by α) the inner mass is equal to M_1^{On} (its modulated mass); this is repeated between $\alpha + \pi$ and $\beta + \pi$. In all other regions, the inner mass is equal to M_1^{Off} (its unmodulated mass). The relationship between these two masses is represented by μ, a non-dimensional number indicating the increased hydrodynamic mass as a fraction of the original mass:

$$\mu = \frac{M_1^{\text{On}} - M_1^{\text{Off}}}{M_1^{\text{Off}}} \tag{6}$$

4.2. Impulse Momentum Considerations

The mass modulation of M_1 is paired with a conservation condition at the boundary $\mathcal{S}$ which models the momentum transfer due to the change in mass. Generally, the change in momentum at a switching boundary is equivalent to an impulse G on the system at that moment:

$$M_1^+ \dot{x}_1^+ - M_1^- \dot{x}_1^- = G$$

Here, $\dot{x}_1^-$ is the velocity at the instant just before the phase flow $(x_1(t), \dot{x}_1(t))$ pierces the switching boundary $\mathcal{S}$ and $\dot{x}_1^+$ is the velocity at the instant just after the phase flow pierces the switching boundary $\mathcal{S}$, with $M_1^{\pm}$ defined similarly. As G is the result of fluid-body interactions that are difficult to characterize analytically, we choose to approximate G as some fraction of the pre-boundary momentum:

$$G = -(1-\epsilon)M_1^- \dot{x}_1^-$$

such that

$$M_1^+ \dot{x}_1^+ = \epsilon M_1^- \dot{x}_1^-$$

where $(1-\epsilon)$ is a (constant) coefficient indicating the amount of momentum loss across $\mathcal{S}$.

By varying ϵ, we may estimate the varying effect of the impulse G without explicitly determining it. In Orazov et al. (2010, 2012) and Rougirel (2013), the case $\epsilon = (1+\mu)$ was exclusively considered. This prescription for ϵ can be questioned on physical grounds because it implies that a positive impulsive force is needed to achieve the mass modulation. Because such an impulsive force is absent in physical realizations of the WEC, we expect that without external momentum impulse $\epsilon \leq 1$. Such a prescription makes sense intuitively, as one would not expect an increase in momentum across any switching boundary without external forcing. With this in mind, we may consider two cases for the switching condition. The first pertains to when the fluid flow is blocked (the mass is modulated):

$$M_1^{\mathrm{On}} \dot{x}_1^+ = \epsilon M_1^{\mathrm{Off}} \dot{x}_1^- \tag{7}$$

When the fluid flow is allowed (the mass is unmodulated), the switching condition is

$$M_1^{\mathrm{Off}} \dot{x}_1^+ = \epsilon M_1^{\mathrm{On}} \dot{x}_1^- \tag{8}$$

This condition pertains to the case when the phase flow passes through the switching boundary $\mathcal{S}$ and the mass changes from M_1^{On} to M_1^{Off}. Finally, we note that the modulation scheme is to be designed such that it is one-directional in phase space. In other words, consulting Figure A.12, for counter-clockwise phase flow the switching is only activated upon crossing $\mathcal{S}$ in a counter-clockwise direction, so any clockwise jumps due to modulation across $\mathcal{S}$ do not affect a modulation.

4.3. Equations of Motion

The equations of motion for the system are, as derived from a balance of linear momentum on the idealization of a two-degree-of-freedom oscillator presented in Figure A.11.

$$\begin{bmatrix} M_1\ddot{x}_1 \\ M_2\ddot{x}_2 \end{bmatrix} + \begin{bmatrix} c_1+c_2 & -c_2 \\ -c_2 & c_2+c_3 \end{bmatrix} \begin{bmatrix} \dot{x}_1 \\ \dot{x}_2 \end{bmatrix} + \begin{bmatrix} k_1+k_2 & -k_2 \\ -k_2 & k_2+k_3 \end{bmatrix} \begin{bmatrix} x_1 \\ x_2 \end{bmatrix} = \begin{bmatrix} F_1 \sin(\omega_f t + \phi) \\ F_2 \sin(\omega_f t) \end{bmatrix} \tag{9}$$

Here ϕ is the phase separation of the forcing F_1 on M_1 relative to the forcing F_2 on M_2. It is convenient to non-dimensionalize (9). To this end, we choose a length scale ℓ and a

stiffness k_1. In a standard fashion, these choices lead to a set of dimensionless variables and parameters:

$$\tilde{x}_\lambda = \frac{x_\lambda}{\ell}, \qquad \tau = \sqrt{\frac{k_1}{M_{2_0}}}t, \qquad \kappa_i = \frac{k_i}{k_1}, \qquad \delta_i = \frac{c_i}{2\sqrt{k_1 M_{2_0}}} \tag{10}$$

$$m_1 = \frac{M_1}{M_{2_0}}, \qquad m_2 = \frac{M_2}{M_{2_0}}, \qquad f_\lambda = \frac{F_\lambda}{k_1 \ell}, \qquad \omega = \sqrt{\frac{M_{2_0}}{k_1}}\omega_f \tag{11}$$

with $i = 1, 2, 3$ and $\lambda = 1, 2$. After some straightforward manipulations, we obtain a set of equations of motion which are equivalent to (9):

$$\begin{bmatrix} m_1 x_1'' \\ m_2 x_2'' \end{bmatrix} + \mathsf{C}\begin{bmatrix} x_1' \\ x_2 \end{bmatrix} + \mathsf{K}\begin{bmatrix} x_1 \\ x_2 \end{bmatrix} = \begin{bmatrix} f_1 \sin(\omega\tau + \phi) \\ f_2 \sin(\omega\tau) \end{bmatrix} \tag{12}$$

In these dimensionless equations, we have dropped the tildes on $x_{1,2}$, the $'$ indicates $\frac{d}{d\tau}$ and

$$\mathsf{K} = \begin{bmatrix} \kappa_1 + \kappa_2 & -\kappa_2 \\ -\kappa_2 & \kappa_2 + \kappa_3 \end{bmatrix}, \qquad \mathsf{C} = \begin{bmatrix} \delta_1 + \delta_2 & -\delta_2 \\ -\delta_2 & \delta_2 + \delta_3 \end{bmatrix} \tag{13}$$

The equations of motion (12) are supplemented by switching conditions at the boundaries $\mathcal{S}$. As a result, the mass parameter m_1 will be state-dependent and we can characterize the equations of motion as an example of a hybrid dynamical system. Such hybrid systems frequently arise in many mechanical systems as outlined in Di Bernardo (2008); Di Bernardo et al. (2008) and Goebel et al. (2009). Within each state, the velocity and accelerations fields are smooth and only at the boundary does a discontinuity result.

4.4. Parameter State Dependance

Before performing simulations of the equations of motion, it is necessary to assign representative values to the parameters in (12). We generally allow the hydrodynamic parameters to be functions of the forcing frequency ω_f (see, e.g., Faltinsen (1990); Sarpkaya (2010)), and the modulation regime, determined by θ. Parameters ν_i affected by the mass-modulated state will be as follows:

$$\nu_i(\theta) \in \mathfrak{V} = \begin{cases} \nu_{i,A} \in \mathfrak{V}_A & \text{if } \theta \in \mathfrak{T}_A \\ \nu_{i,0} \in \mathfrak{V}_0 & \text{if } \theta \in \mathfrak{T}_0 \end{cases} \tag{14}$$

where $\nu_{i,A}$ is the i-th parameter in the mass-modulated regime, $\nu_{i,0}$ is the i-th parameter in the rest mass regime, $\mathfrak{V}_A$ is the set of all parameters in the mass-modulated regime, $\mathfrak{V}_0$ is the set of all parameters in the rest mass regime, and $\mathfrak{V}$ is the set of all parameters which depend on θ.

To determine the explicit ω_f and θ dependance of hydrodynamic parameters ν_i, we enlisted the assistance of a hydrodynamic modeling software commonly used on marine structures, ANSYS AQWA. This software twice analyzed the simple model shown in Figure A.11 above, via Euler's equations, subjected to an incident wave forcing of frequency ω_f for the geometry seen in Appendix A. In the first analysis, the response of the masses was considered separately, and in the second, they were considered together.

The effective masses of the inner M_1 and outer M_2 floats will vary depending on the state of modulation and the forcing frequency, so they are $\in \mathfrak{V}$, and accordingly:

$$M_j = M_{j_0} + M_j^{EI}(\theta, \omega_f), \qquad j = 1, 2 \tag{15}$$

where M_{j_0} is the rest mass of float j and $M_j^{EI}(\theta, \omega_f)$ is the effective increase in mass of float j. From the AQWA simulation where the masses were considered separately, seen in Figure A.13, it became evident that $M_1^{EI}(\theta, \omega_f)$ was a very weak function of ω_f, so explicit dependance on the forcing frequency was removed, thereby simplifying to

$$M_1^{EI}(\theta) = \begin{cases} M_{1_A}^{EI} & \text{if } \theta \in \mathfrak{T}_A \\ M_{1_0}^{EI} & \text{if } \theta \in \mathfrak{T}_0 \end{cases} \tag{16}$$

where, after neglecting the weak ω_f dependance, $M_{1_A}^{EI}$ and $M_{1_0}^{EI}$ are constants (the mean values of $M_{1_A}^{EI}(\omega_f)$ and $M_{1_0}^{EI}(\omega_f)$ respectively). With this simplification, μ may be determined recalling (6):

$$\mu = \frac{M_1^{\text{On}} - M_1^{\text{Off}}}{M_1^{\text{Off}}} = \frac{(M_{1_0} + M_{1_A}^{EI}) - (M_{1_0} + M_{1_0}^{EI})}{M_{1_0} + M_{1_0}^{EI}}.$$

Hence μ represents a ratio of effective masses:

$$\mu = \frac{M_{1_A}^{EI} - M_{1_0}^{EI}}{M_{1_0} + M_{1_0}^{EI}}. \tag{17}$$

This representation of μ pertains to realizations such as the one shown in Figure A.3(i)[1]. That is, μ is equal to the difference in the hydrodynamic added mass of M_1 when the flaps are in the open state compared to the closed state. From the AQWA analysis where the floats were considered together, $M_1^{EI}(\theta, \omega_f)$ was verified to still be a weak function of ω_f. We assumed then, for a fixed M_{1_0}, that by altering the geometry or size of the lower float the desired μ could be achieved.

Additionally, from both AQWA analyses, $M_2^{EI}(\theta, \omega_f)$ was found to be a linearly decreasing function of ω_f, as seen in Figure A.13, with a very weak dependance on the state of mass modulation and thus weak dependance on θ, thereby simplifying to:

$$M_2^{EI}(\theta, \omega_f) = \begin{cases} M_{2_A}^{EI}(\omega_f) & \text{if } \theta \in \mathfrak{T}_A \\ M_{2_0}^{EI}(\omega_f) & \text{if } \theta \in \mathfrak{T}_0 \end{cases} \tag{18}$$

The regime dependance of other dynamical elements in the system was determined from the AQWA where the masses were considered together. The spring k_1 and dashpot c_1 represent the buoyancy force and hydrodynamic damping on the mass M_1. Although k_1 is a constant, c_1 depends on whether the flaps are open/closed and the frequency ω_f of the incident waves, so $c_1 \in \mathfrak{V}$. The second spring-dashpot system represents the PTO and the coupling between the masses. In general, hydrodynamic $k_2 \approx 0$, B represents the

[1]The corresponding representation of μ for realizations such as the one shown in Figure A.3(ii) is straightforward to infer.

damping of the PTO, and c_2' represents hydrodynamic damping (≈ 0, removing regime and frequency dependance) and any additional mechanical damping not encompassed in the PTO, and thus $c_2' \notin \mathfrak{V}$. Finally, the spring k_3 and dashpot c_3 represent the buoyancy force and hydrodynamic damping on the mass m_2. We assume that k_3 is constant while c_3 is a function of ω_f. Neither parameter is assumed to depend on the configuration of the flaps. In summary:

$$c_1 = c_1(\theta, \omega_f) \in \mathfrak{V}, \qquad c_2 = c_2(c_2', B) \notin \mathfrak{V}, \qquad c_3 = c_3(\omega_f) \notin \mathfrak{V}. \tag{19}$$

Accordingly, in performing the nondimensional numerical analyses contained below, we used the relevant mass, stiffness, and damping terms defined from the AQWA analysis, where relevant, and allowed μ to vary as a parameter: the specific values for these mass, stiffness, and damping terms is contained in Appendix A.

5. Metrics for Energy Harvesting

As in works on resonant energy harvesters (see, e.g., Diamond et al. (2013); Falnes (1999); Orazov et al. (2010, 2012); Stephen (2006); Tang and Zuo (2011)), we take the power generated by our WEC as proportional to the velocity across the PTO device. As such, the nondimensional average power that can be harnessed from the harvester is defined as

$$\mathrm{P} = \frac{B}{2T\sqrt{k_1 M_{2_0}}} \int_0^T \left(x_2' - x_1'\right)^2 \mathrm{d}\tau \tag{20}$$

where T is a (nondimensional) period of integration which is much larger than the forcing period $\frac{2\pi}{\omega}$. The power P is generally a function of many parameters; if one determines m_i, κ_i, and δ_i from the AQWA analysis, it reduces to dependence upon ℓ (a suitable length scale), F_α, ω_f, δ_2, μ, ϵ, ϕ, and switching boundaries α and β.

For a single degree-of-freedom linear mechanical systems, one has a resonant frequency ω_r and an associated damping c and natural frequency ω_n. If one wishes to optimally harvest energy using such a system, then it is known that one tunes ω_n to coincide with the incident frequency and then B is chosen so that $B = c$. For two-degree-of-freedom systems such as shown in Figure A.11, the optimal system parameters must be determined numerically. For our case, we choose a PTO damping B that is equivalent to the mechanical and hydrodynamic damping c_2': hence $c_2 = B + c_2' = 2c_2'$.

Selecting the optimal α and β (both equal to $\frac{\pi}{2}$ as in Diamond et al. (2013) and illustrated schematically in Figure A.3) further reduced the problem - cf. Figures A.2, A.14 and A.15. In searching for optimal values for the remaining parameters in the system, we found that the effects of changing the values of M_{1_0}, M_{2_0}, k_1, and k_2 on power harvesting could be most easily interpreted using a tuning parameter γ. This parameter, as in Tang and Zuo (2011), is defined as a ratio of frequencies:

$$\gamma = \frac{\omega_{n,1}}{\omega_{n,2}}, \tag{21}$$

where

$$\omega_{n,1} = \sqrt{\frac{k_1}{M_{1_0}}}, \qquad \omega_{n,2} = \sqrt{\frac{k_2}{M_{2_0}}}. \tag{22}$$

6. Optimal Energy Harvesting

A numerical code was developed to evaluate P (cf. (20)) over a multi-parameter space consisting of ω, γ, δ_2, μ, f_1, f_2, ϵ, ϕ, α and β; this code allowed for ranges of three parameter subsets to be investigated while all other parameters remained single valued. The resulting values of P could then be plotted, with two of the parameters of interest corresponding to the x and y axis (the z axis always corresponding to P) and the third parameter of interest encompassed in time or in multiple plots.

It should be noted that the phase separation ϕ between the forcing on M_1 and M_2 was chosen to be zero in all simulations. This was dually motivated: firstly, zero phase separation is the most conservative assumption with respect to the harvested power. As this quantity is directly related to the square of the relative velocity, any phase separation increase above zero would naturally result in an increase in harvested power, and we were keen to study the effect of mass modulation independent of this tendency. Secondly, choosing a specific phase separation would be arbitrary and unmotivated, even without the first restriction, as we had no good estimate of what it would realistically be.

Here, the first two parameters were regularly chosen to be ω and μ: ω ranges allowed for easy comparison in the frequency space, which was almost always desirous, and μ ranges allowed for similar comparisons in added mass space (importantly including $\mu = 0$, the nominal case).

Although switching boundaries α and β were previously found to be optimal when set to $\frac{\pi}{2}$ in previous work (Diamond et al., 2013), it was not definitively known if this would be the case for the current model. As such, verification of these parameters' optimality was first investigated. It was verified that the prescription $\alpha = \frac{\pi}{2}$ and $\beta = \frac{\pi}{2}$ was, in fact, optimal in the two mass case as well (cf. Figures A.14 and A.15). This was to be expected, as these parameters only affect one mass in this model as they did previously; an intuitive explanation for optimality is discussed in Diamond et al. (2013) and is not repeated here. Interestingly, while certain values of added mass onset α completely negate any advantage the added mass scheme has over the nominal case, identical selections of added mass length β do not. Rather than resulting in higher P for increasing values of μ, these selections resulted in a shift of the dominant resonant peak at $\omega = \omega_r$, with a P on the order of magnitude of the nominal case, for increasing values of μ: cf. Figure A.16.

The momentum coefficient ϵ was devised so we could investigate the effect of impulse G, as we do not generally know G from first principles alone - it must be determined experimentally. We would expect that larger ϵ, or minimized momentum loss, would correspond to more robust peaks in P than smaller ϵ, or unminimized momentum loss, would. Examining Figure A.17, we see that this is indeed the case; more usefully, the simulation informs us that below a certain critical value of ϵ (which generally varies as a function of the other parameters) the mass modulation produces a reduced P than corresponding value of P for the nominal case.

Tuning parameter γ, the ratio of the switching mass's natural frequency to the buoy mass's natural frequency, is also of interest. With non-dimensionalized driving frequency ω as given in (11), we would expect that altering γ would shift ω in some way. Specifically how changing γ would affect P was not known. As can be seen in Figure A.18, increasing γ does have the expected result of increasing ω_r; additionally, we can see that the peak

value of P increases with γ up to a certain point, here at about $\gamma = 1.5$, after which increasing γ has no effect on the peak power. This suggests that there is an optimal range of γ, above some critical value, where P is unaffected by increasing choices of $\omega_{n,1}$.

As has been mentioned previously, we narrowed our investigation of the effect of damping δ_2 by selecting $B = c_2'$. With this selection, we would expect that increasing δ_2 up to some value would similarly increase the maximum P, as it is proportional to δ_2. Beyond this point, however, the potential benefit of higher PTO damping would be unrealized as the increased overall damping would limit the velocity between the masses and thus the collected power. This trend was verified and can be seen in Figure A.19: beyond $\delta_2 = 0.05$ (in this case) the ridge of peak P is broadened and reduced with increasing choices of δ_2. This suggests an optimal choice of δ_2 exists for any given set of parameters.

The parameters whose effects are the most difficult to comprehend are the forcings f_1 and f_2. Their values, both relative to each other and outright, are not well known from a purely dynamical standpoint and experimentation is necessary to specify them. Despite this, a few things may be gleaned from the numerical simulations, cf. Figures A.20 and A.21. The most important takeaway is that, with the other forcing fixed, increasing the direct forcing on mass one (f_1) has a much greater effect on P than increasing that on mass two (f_2). This is problematic as f_2 is more likely to be easily determined than f_1 in practice. Further, f_2 corresponds to the forcing on the buoy mass directly excited by the incident waves - but f_1 seems more critical to the WEC's operation.

7. Conclusions

Experimental work on a modified WEC specified in Diamond et al. (2013) was performed to validate the proposed optimal mass modulation contained therein. It was found that the addition of mass modulation was realizable - as was the mass modulation specified in Orazov et al. (2010, 2012) and tested in Orazov (2011) - and this new scheme improved the power harvested by the WEC significantly for a wide range of incident wave frequencies: moreover, it was found to only be slightly worse than the case without mass modulation at one testing frequency, which itself was significantly above the fundamental frequency of the prototype. Regardless, we devised a more robust analysis of a buoy-type WEC to affect a sensitivity analysis of the mass-modulation scheme to a variety of design and environmental parameters that would be rather difficult, if not impossible, to change on a prototype WEC. Accordingly, we introduced a two-degree-of-freedom model that would more realistically reflect the dynamics of a buoy-type WEC. Using this more realistic model for the WEC we have shown the potential energy harvesting benefits of the mass-modulation scheme. For example, the model shows that it is possible to increase the harvesting capabilities by 200% in some instances (cf. Figure A.22). It should be emphasized that the effectiveness of the modulation scheme is heavily dependent on the amount of fluid momentum carried across the switching boundary. In particular, if the design of the WEC is such that ϵ is too small, then the mass-modulation scheme does not result in significant improvements over the nominal case and may indeed be detrimental.

In closing we wish to emphasize that the results shown in the paper verify that the mass modulation scheme is effective. Furthermore, the modulation scheme we are proposing can be easily generalized - all that is required is to change the hydrodynamic added mass (with or without trapping water) of the inner float. Broadly, one can achieve mass modulation using induced mass (virtual mass) by changing the shape of the inner float cyclically. The flaps we have in our experiments are but one realization of this idea. It is not too difficult to conceive of other realizations - some of which can be achieved using active control.

Acknowledgements

This research was partially supported by grant number CMMI-1000906 from the U. S. National Science Foundation. We would also like to thank Steffen Paiva, who assisted greatly in the realization of the experiments contained in this paper and the reviewers of an earlier draft of this paper for their constructive comments.

References

Babarit, A., Duclos, G., Clément, A., 2004. Comparison of latching control strategies for a heaving wave energy device in random sea. Applied Ocean Research 26, 227–238.

Daqaq, M.F., Masana, R., Erturk, A., Quinn, D.D., 2014. On the role of nonlinearities in vibratory energy harvesting: A critical review and discussion. ASME Applied Mechanics Reviews 66, 6040801.

Di Bernardo, M., 2008. Piecewise-Smooth Dynamical Systems: Theory and Applications. Springer Verlag.

Di Bernardo, M., Budd, C., Champneys, A., Kowalczyk, P., Nordmark, A., Tost, G., Piiroinen, P., 2008. Bifurcations in nonsmooth dynamical systems. SIAM Review 50, 629–701.

Diamond, C., O'Reilly, O.M., Savaş, Ö., 2013. The impulsive effects of momentum transfer on the dynamics of a novel ocean wave energy converter. Journal of Sound and Vibration 332, 5559–5565.

Dick, W., 2005. Wave energy converter. U.S. Patent number 6857266, issued in February 2005.
Evans, D.V., 1976. A theory for wave-power absorption by oscillating bodies. J. Fluid Mech. 77, 1–25.
Evans, D.V., 1982. Wave-power absorption by systems of oscillating surface pressure distributions. J. Fluid Mech. 114, 481–499.
Falcão, A.F.O., Cândido, J.J., Justino, P.A.P., Henriques, J.C.C., 2012. Hydrodynamics of the IPS buoy wave energy converter including the effect of non-uniform acceleration tube cross section. Renewable Energy 41, 105–114.
Falnes, J., 1999. Wave energy conversion through relative motion between two single-mode oscillating bodies. Journal of Offshore Mechanics and Arctic Engineering 121, 32–39.
Falnes, J., 2002. Optimum control of oscillation of wave-energy converters. International Journal of Offshore and Polar Engineering 12, 147–155.
Faltinsen, O.M., 1990. Sea Loads on Ships and Offshore Structures. Cambridge University Press, Cambridge, U.K.
Goebel, R., Sanfelice, R., Teel, A., 2009. Hybrid dynamical systems. IEEE Control Systems Magazine 29, 28–93.
Goggins, J., Finnegan, W., 2014. Shape optimisation of floating wave energy converters for a specified wave energy spectrum. Renewable Energy 71, 208–220.
McCabe, A., 2013. Constrained optimization of the shape of a wave energy collector by genetic algorithm. Renewable Energy 51, 274 – 284.
Mei, C.C., 1976. Power extraction from water waves. J. Ship Research 20, 63–66.
Olvera, A., Prado, E., Czitrom, S., 2007. Parametric resonance in an oscillating water column. Journal of Engineering Mathematics 57, 1–21.
Orazov, B., 2011. A Novel Excitation Scheme for an Ocean Wave Energy Converter. Ph.D. thesis. University of California at Berkeley.
Orazov, B., O'Reilly, O.M., Savaş, Ö., 2010. On the dynamics of a novel ocean wave energy converter. Journal of Sound and Vibration 329, 5058–5069.
Orazov, B., O'Reilly, O.M., Zhou, X., 2012. On forced oscillations of a simple model for a novel wave energy converter: non-resonant instability, limit cycles, and bounded oscillations. Nonlinear Dynamics 67, 1135–1146.
Rhoads, J.F., Miller, J.N., Shaw, S.W., Feeny, B.F., 2008. Mechanical domain parametric amplification. Journal of Vibration and Acoustics 130, 061006–1–061006–7.
Rougirel, A., 2013. Mathematical analysis of a wave energy converter model. Nonlinear Analysis: Real World Applications 14, 434–454.
Rugar, D., Grütter, P., 1991. Mechanical parametric amplification and thermomechanical noise squeezing. Physical Review Letters 67, 699–702.
Salter, S.H., 1974. Wave power. Nature 249, 720–724.
Sarpkaya, T., 2010. Wave Forces on Offshore Structures. Cambridge University Press, Cambridge, U.K.
Stephen, N.G., 2006. On energy harvesting from ambient vibration. Journal of Sound and Vibration 293, 409–425.
Tang, X., Zuo, L., 2011. Enhanced vibration energy harvesting using dual-mass systems. Journal of Sound and Vibration 330, 5199–5209.
Vicente, P. C. Falcão, A.F.O., Justino, P.A.P., 2013. Nonlinear dynamics of a tightly moored point-absorber wave energy converter. Ocean Engineering 59, 20–36.
Wirkus, S., Rand, R., Ruina, A., 1998. How to pump a swing. The College Mathematics Journal 29, 266–275.
Yeung, R.W., Peiffer, A., Tom, N., Matlak, T., 2011. Design, analysis, and evaluation of the UC-Berkeley wave-energy extractor. Journal of Offshore Mechanical and Arctic Engineering 134, 021902.
Zurkinden, A., Ferri, F., Beatty, S., Kofoed, J., Kramer, M., 2014. Non-linear numerical modeling and experimental testing of a point absorber wave energy converter. Ocean Engineering 78, 11–21.

Appendix A. Numerically Determined Hydrodynamic Values

Recalling our dimensioned mass equations (15), (16) and (18):

$$
\begin{aligned}
M_j =& M_{j_0} + M_j^{EI}(\theta, \omega_f), \qquad j = 1, 2 \\
M_1^{EI}(\theta) =& \begin{cases} M_{1_A}^{EI} & \text{if } \theta \in \mathfrak{T}_A \\ M_{1_0}^{EI} & \text{if } \theta \in \mathfrak{T}_0 \end{cases} \\
M_2^{EI}(\theta, \omega_f) =& \begin{cases} M_{2_A}^{EI}(\omega_f) & \text{if } \theta \in \mathfrak{T}_A \\ M_{2_0}^{EI}(\omega_f) & \text{if } \theta \in \mathfrak{T}_0 \end{cases}
\end{aligned}
$$

AQWA analysis was performed on the (coupled) geometry seen in Figures A.24 and A.25, where Figure A.24 represents the system with M_1 in the modulated (M_1^{On}) state and Figure A.25 represents the system with M_1 in the unmodulated (M_1^{Off}) state. It was determined using this AQWA analysis that for our example geometry, with a limited frequency range $\omega_f \in [0.3\pi, 0.5\pi]$ Hz,

$$
\begin{aligned}
M_{1_0} &= 18247.81 \text{ kg} \\
M_{1_A}^{EI}(\omega_f) &= -1052.6 \text{ kg/Hz} \cdot \left(\tfrac{\omega_f}{2\pi}\right) + 13838 \text{ kg} \\
M_{1_0}^{EI}(\omega_f) &= -2030 \text{ kg/Hz} \cdot \left(\tfrac{\omega_f}{2\pi}\right) + 4197.5 \text{ kg}
\end{aligned} \tag{A.1}
$$

Notice that, for the range of frequencies here, this means $M_{1_A}^{EI}(\omega_f)$ decreases from 13680.11 kg to 13574.85 kg. Such are variances of $\pm 0.386\%$ from the mean value of 13627.48 kg. Similarly, for $M_{1_0}^{EI}(\omega_f)$ we see a decrease from 3893.3 kg to 3690.3 kg. Such are variances of $\pm 2.677\%$ from the mean value of 3791.8 kg. So the simplification in (16) of $M_{1_A}^{EI}(\omega_f) \to M_{1_A}^{EI}(= 13627.48\text{kg, here})$ and $M_{1_0}^{EI}(\omega_f) \to M_{1_0}^{EI}(= 3690.3\text{kg, here})$ is justified.

We may also look at the dependance of μ on ω_f, if we had not made the simplification of (16) that led to (17), so

$$
\mu(\omega_f) = \frac{M_{1_A}^{EI}(\omega_f) - M_{1_0}^{EI}(\omega_f)}{M_{1_0} + M_{1_0}^{EI}(\omega_f)} \to \frac{977.4 \text{ kg/Hz} \cdot \left(\tfrac{\omega_f}{2\pi}\right) + 9640.5 \text{ kg}}{-2030 \text{ kg/Hz} \cdot \left(\tfrac{\omega_f}{2\pi}\right) + 22445.31 \text{ kg}}
$$

which increases from 0.442 to 0.451, which are variances of -0.954% and 0.960% (respectively) from the mean value of 0.446. Notably, using the simplified expression for μ (17), we get $\mu = 0.446$ as well.

For the values associated with the second mass, it was determined that:

$$
\begin{aligned}
M_{2_0} &= 15292.09 \text{ kg} \\
M_{2_A}^{EI}(\omega_f) &= -195789 \text{ kg/Hz} \cdot \left(\tfrac{\omega_f}{2\pi}\right) + 97808 \text{ kg} \\
M_{2_0}^{EI}(\omega_f) &= -185100 \text{ kg/Hz} \cdot \left(\tfrac{\omega_f}{2\pi}\right) + 96225 \text{ kg}
\end{aligned} \tag{A.2}
$$

For the damping parameters, we find that

$$
c_1(\theta, \omega_f) = \begin{cases} 263.16 \text{ kg/(Hz} \cdot \text{s)} \cdot \left(\tfrac{\omega_f}{2\pi}\right) + 216.53 \text{ kg/s} & \text{if } \theta \in \mathfrak{T}_A \\ -480 \text{ kg/(Hz} \cdot \text{s)} \cdot \left(\tfrac{\omega_f}{2\pi}\right) + 391 \text{ kg/s} & \text{if } \theta \in \mathfrak{T}_0 \end{cases} \tag{A.3}
$$

$$
c_3(\theta, \omega_f) = \begin{cases} 309473.6 \text{ kg/(Hz} \cdot \text{s)} \cdot \left(\tfrac{\omega_f}{2\pi}\right) - 18591.1 \text{ kg/s} & \text{if } \theta \in \mathfrak{T}_A \\ 314700 \text{ kg/(Hz} \cdot \text{s)} \cdot \left(\tfrac{\omega_f}{2\pi}\right) - 21475 \text{ kg/s} & \text{if } \theta \in \mathfrak{T}_0 \end{cases} \tag{A.4}
$$

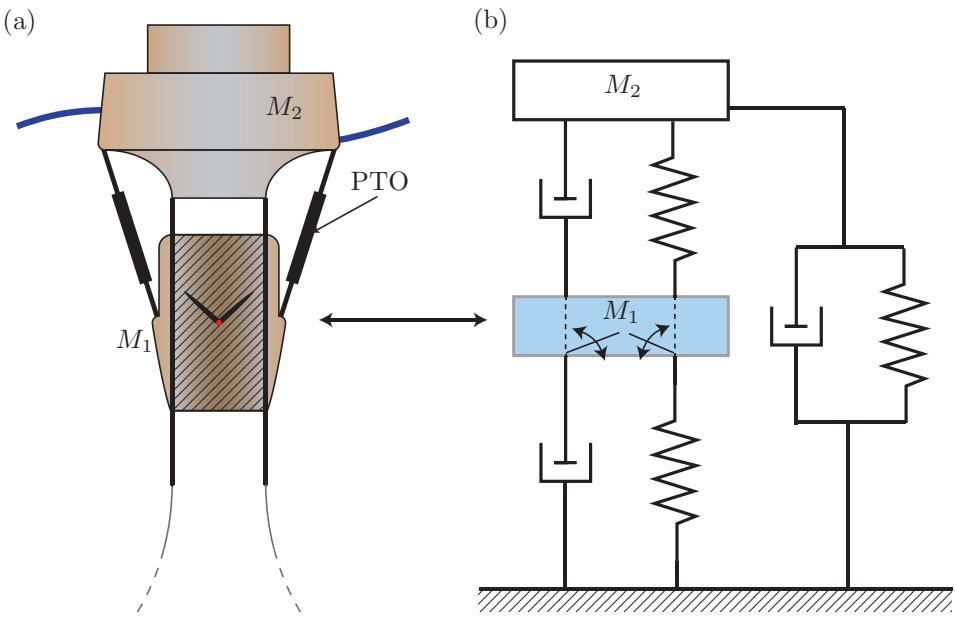

Figure A.1: (a) Schematic of a heaving buoy type WEC featuring modulation of the mass M_1. The motion of M_1 relative to M_2 is used by the PTO to generate electricity. In the interests of clarity, several details, including the tethering mechanism, are not shown. In (b), a two degree-of-freedom model for this WEC is shown with various (hydrodynamic and mechanical) dampings and stiffnesses. Note that the mass M_1 in this model varies with time.

And for the stiffnesses, we find that

$$k_1 = 46.7791\,\mathrm{kN/m}, \qquad k_3 = 330.6602\,\mathrm{kN/m}. \tag{A.5}$$

Table A.1: Comparison of the experimental velocities for Scheme III at the six testing frequencies. $\Delta v = v_i - v_o$, where v_i is the inner mass velocity and v_o is the outer mass velocity; additionally, the subscript "no flaps" indicates testing without modulation, and the subscript "flaps" indicates testing with modulation. The superscript "RMS" indicates and average by root-mean-square, or $f(t)^{\mathrm{RMS}} = \sqrt{\frac{1}{T_f - T_0} \int_{T_0}^{T_f} f(\tau)^2 \, d\tau}$

f (Hz)	$\Delta v^{\mathrm{RMS}}_{\text{no flaps}}$ (m/s)	$\Delta v^{\mathrm{RMS}}_{\text{flaps}}$ (m/s)	$v_{\mathrm{i}}{}^{\mathrm{RMS}}_{\text{no flaps}}$ (m/s)	$v_{\mathrm{i}}{}^{\mathrm{RMS}}_{\text{flaps}}$ (m/s)
0.650	0.050	0.122	0.177	0.203
0.675	0.057	0.122	0.193	0.189
0.725	0.082	0.098	0.229	0.225
0.750	0.073	0.141	0.207	0.257
0.800	0.099	0.099	0.254	0.202
0.850	0.112	0.125	0.251	0.212

Table A.2: Comparison of the experimental velocities for Scheme I at the five testing frequencies. $\Delta v = v_i - v_o$, where v_i is the inner mass velocity and v_o is the outer mass velocity; additionally, the subscript "no flaps" indicates testing without modulation, and the subscript "flaps" indicates testing with modulation. The superscript "RMS" indicates and average by root-mean-square, or $f(t)^{\mathrm{RMS}} = \sqrt{\frac{1}{T_f - T_0} \int_{T_0}^{T_f} f(\tau)^2 \, d\tau}$

f (Hz)	$\Delta v^{\mathrm{RMS}}_{\text{no flaps}}$ (m/s)	$\Delta v^{\mathrm{RMS}}_{\text{flaps}}$ (m/s)	$v_{\mathrm{i}}{}^{\mathrm{RMS}}_{\text{no flaps}}$ (m/s)	$v_{\mathrm{i}}{}^{\mathrm{RMS}}_{\text{flaps}}$ (m/s)
0.60	0.041	0.038	0.122	0.118
0.64	0.059	0.065	0.132	0.135
0.68	0.075	0.086	0.137	0.138
0.72	0.117	0.118	0.151	0.169
0.76	0.117	0.086	0.141	0.171

Table A.3: Comparison of the average phase lag $\bar{\tau}$ of the inner mass velocity v_i relative to the outer mass velocity v_o and the root-mean-square (RMS) power P generated by the PTO for Scheme III at the six testing frequencies. The subscript "no flaps" indicates testing without modulation, and the subscript "flaps" indicates testing with modulation. The superscript "RMS" indicates and average by root-mean-square, or $f(t)^{\mathrm{RMS}} = \sqrt{\frac{1}{T_f - T_0} \int_{T_0}^{T_f} f(\tau)^2 \, d\tau}$

f (Hz)	$\bar{\tau}_{\text{no flaps}}$ (s)	$\bar{\tau}_{\text{flaps}}$ (s)	$\mathrm{P}^{\mathrm{RMS}}_{\text{no flaps}}$ (W)	$\mathrm{P}^{\mathrm{RMS}}_{\text{flaps}}$ (W)
0.650	0.063	0.090	1.251	2.467
0.675	0.063	0.133	1.387	2.541
0.725	0.070	0.077	1.826	2.139
0.750	0.070	0.091	1.675	2.802
0.800	0.070	0.084	2.193	2.173
0.850	0.077	0.084	2.395	2.620

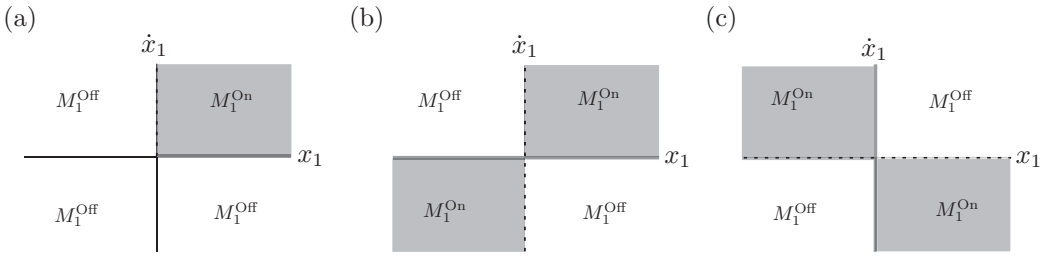

Figure A.2: Three examples of mass-modulation schemes denoted respectively as (a), Scheme I, (b) Scheme II, and (c) Scheme III. Scheme I is featured in the experimental work in Orazov (2011), Scheme II is the case considered in Orazov et al. (2010, 2012) and Rougirel (2013), and Scheme III is an optimal energy harvesting scheme considered here and in Diamond et al. (2013).

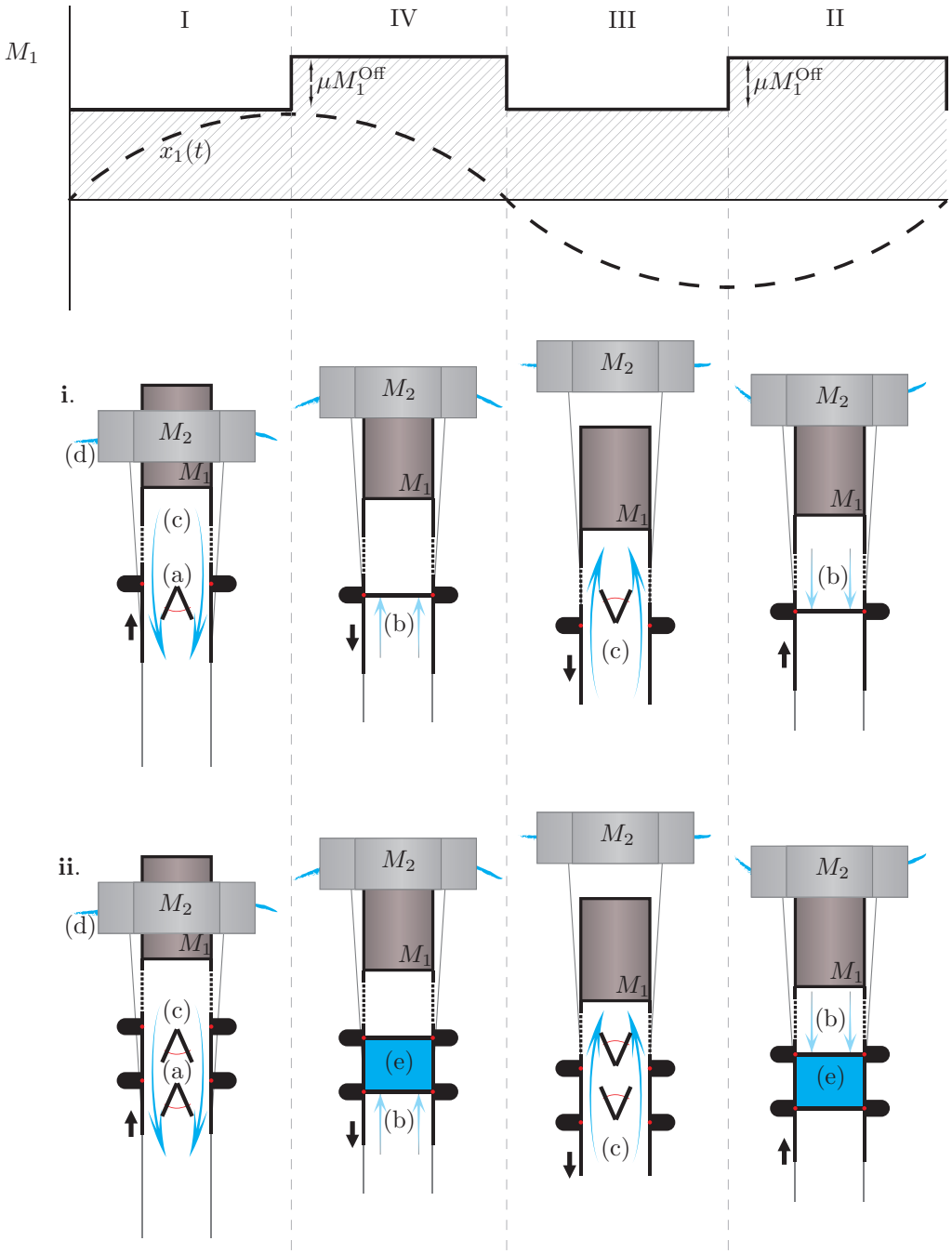

Figure A.3: Illustration of the mass-modulation scheme III. In the top part of the figure, the idealized modulated mass is a fraction μ of the baseline mass M_1^{Off} and is a function of position x_1 and velocity $\dot{x}_1$ of the inner float. In the bottom portion of the figure, we see two means of achieving the mass modulation μM_1^{Off}: in **i**. utilizing only hydrodynamic added mass and in **ii**. utilizing both hydrodynamic added mass and entrapped water mass. Elements of note are an outer float of mass M_2, a (primarily) submerged inner float (featuring a hollow open ended cylinder) of mass M_1, (a) mass-modulation control flaps, (b) impeded water flow, (c) unimpeded water flow, (d) water surface, and (e) trapped water mass.

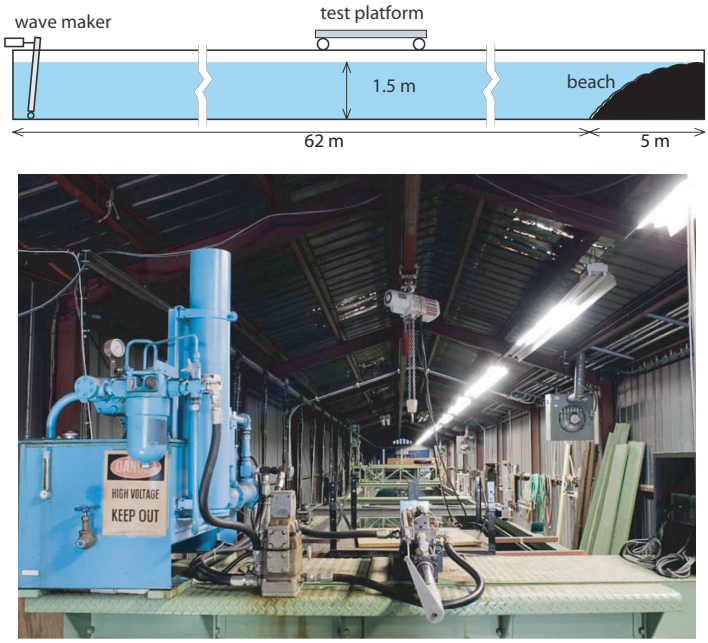

Figure A.4: UC Berkeley Tow Tank facility in Richmond, CA. Schematic (top) and image of the facility with the wavemaker mechanism seen in blue in the foreground (bottom).

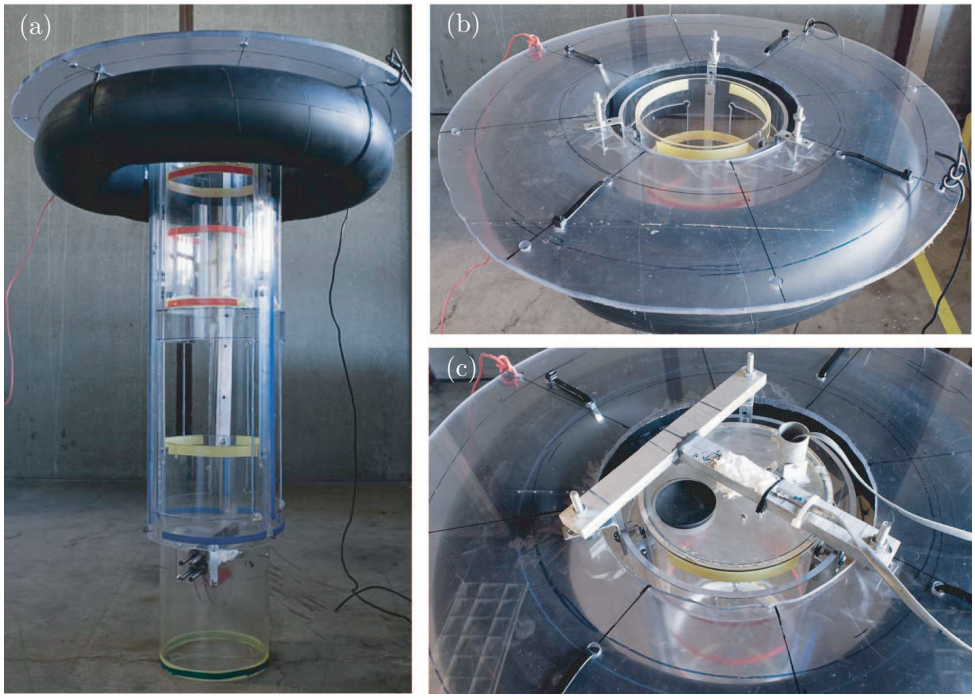

Figure A.5: Images of the original scale prototype WEC. (a) Assembly: outer float, inner float and the water entrapment system; (b) outer float with the inner float visible (marked by yellow tape); (c) 3-axis accelerometers rigidly mounted to the outer (top of the T-beam) and inner (center of the upper cap) floats. The signal cables are connected to a land-based Arduino microcontroller.

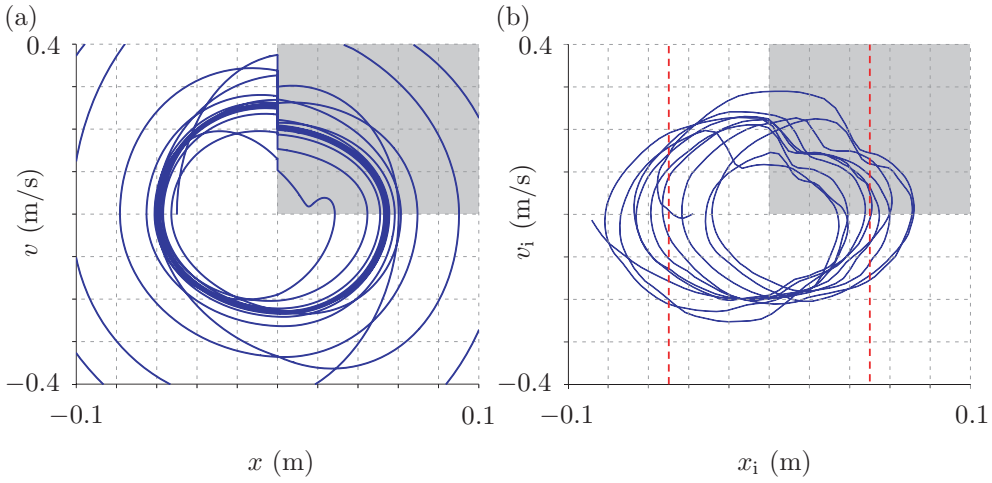

Figure A.6: (a) Dimensional output of simulation of one degree-of-freedom model in (Diamond et al., 2013, Eqns. (1)–(4)) with switching boundary momentum loss; specific parameter values utilized are: $f = 0.25$, $\omega_f = 0.68$, $\omega_n = 6$, $\mu = 0.45$, $\delta = 0.07$, ϵ (momentum loss coefficient)$= 0.8$, $\ell = 0.1$. (b) Experimental data from Orazov (2011) of the inner float position x_i versus the inner float velocity v_i for a wave excitation frequency 0.68 Hz, with flaps installed (i.e., with added mass effects). The dashed vertical lines mark ± 5cm, corresponding to the 10 cm peak-to-peak input wave amplitude.

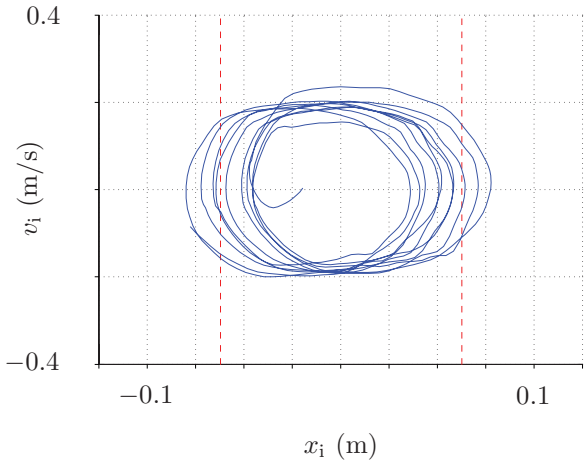

Figure A.7: Experimental data of inner float position x_i vs. inner float velocity v_i for a wave excitation frequency of 0.68 Hz without flaps installed (i.e., without mass modulation). The dashed vertical lines mark ± 5cm, corresponding to the 10 cm peak-to-peak wave amplitude.

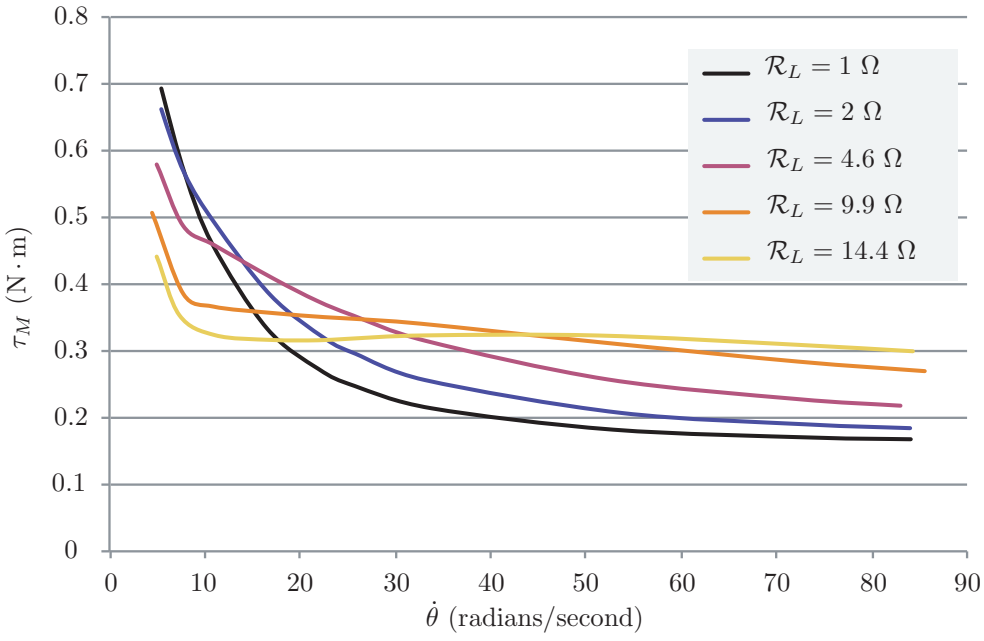

Figure A.8: Angular speed-torque $\left(\dot{\theta}, \tau_M(\dot{\theta}; \mathcal{R}_L)\right)$ curves for the Slo-Syn M062-FC-404B stepper motor used as a PTO in the experiment, for a variety of different load resistances $\mathcal{R}_L$. Restricting attention to the area of low rotational speeds ($\approx<$ 10 radians/second), we observe that the torque τ_M decreases, and the magnitude of the torque/rotational speed proportionality constant increases, with increasing $\mathcal{R}_L$.

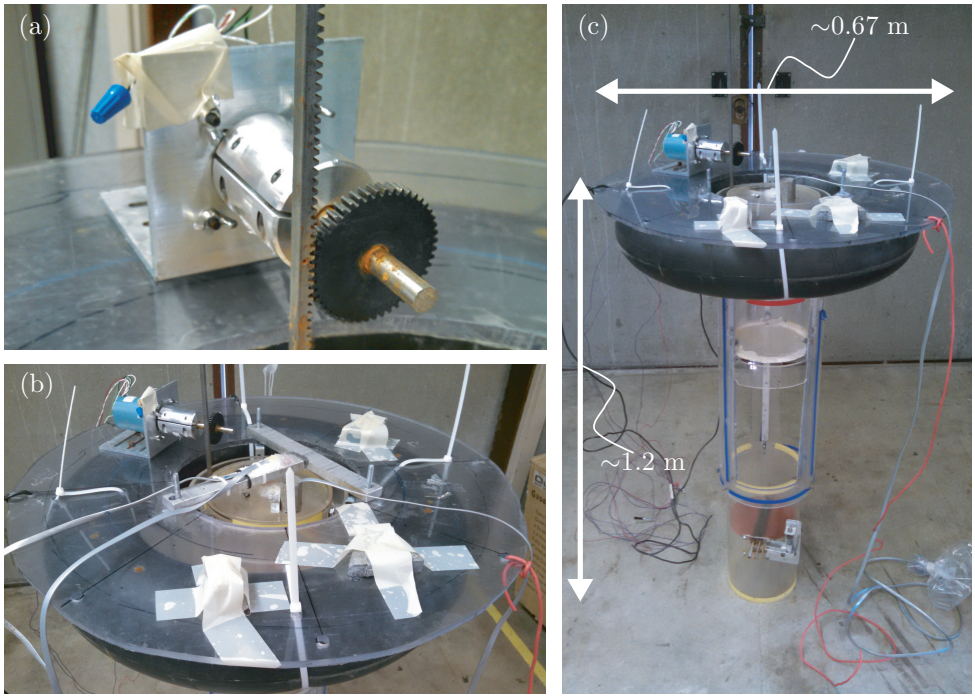

Figure A.9: Images of the current scale prototype WEC with updates. (a) The implemented PTO; (b) Accelerometers mounted to the outer and inner floats, as before, with addition of PTO and necessary counterweights; (c) Assembly, showing addition of PTO and updated flap mechanism.

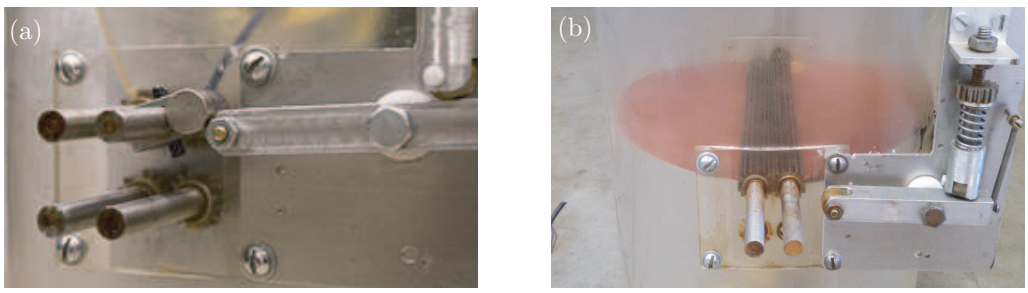

Figure A.10: Flap mechanisms used in experiments to approximate (a) Scheme I and (b) Scheme III. In the former, a spring force resists the fluid pressure until mass modulation is desired. In the latter, contact force between the rubber at the edges of the flaps and the cylinder wall resists the fluid pressure until mass modulation is desired.

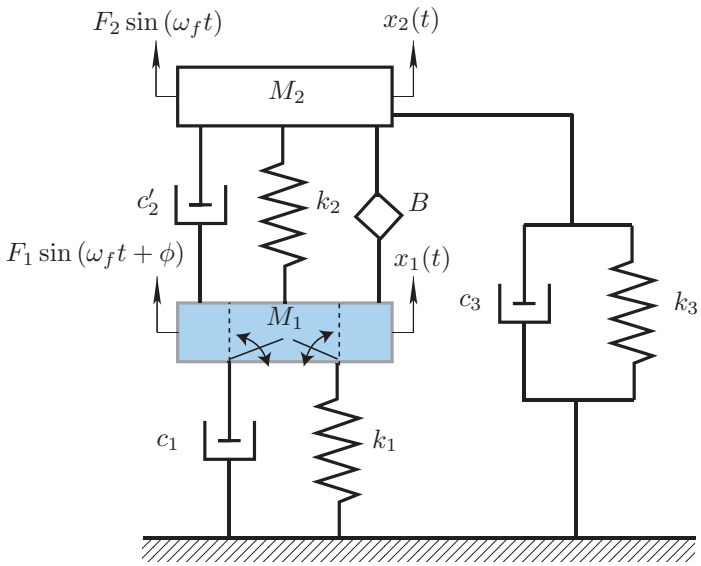

Figure A.11: The two-degree-of-freedom linear oscillator. The mass M_1 of the inner float varies depending on the sign of $x_1 \frac{dx_1}{dt}$ and this mass modulation is achieved using a set of flaps inside the inner float.

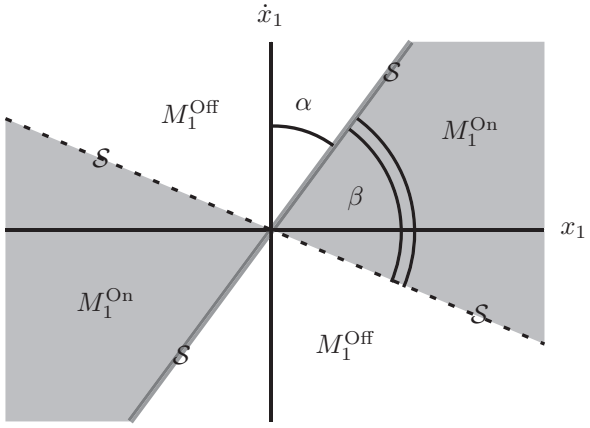

Figure A.12: The mass M_1 varies depending on the sign of x_1 and $\dot{x}_1$: $M_1 = M_1^{\text{On}}$ (in the modulated mass region) or $M_1 = M_1^{\text{Off}}$ (in the unmodulated mass region). The most general case is shown; the rays $\mathcal{S}$ correspond to the locations in the state space where water is either trapped or released.

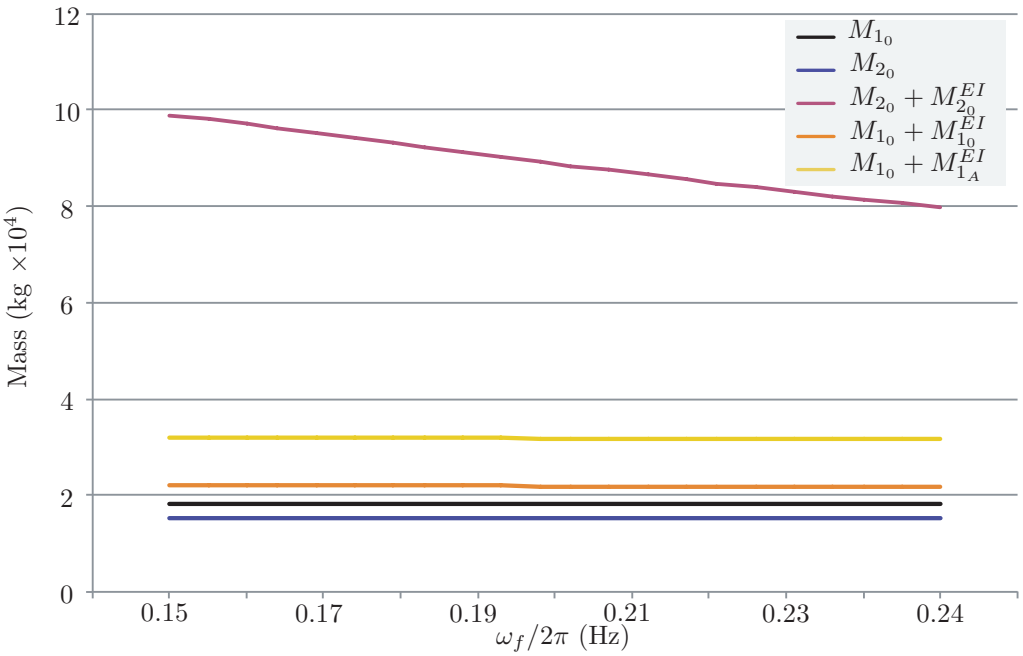

Figure A.13: AQWA simulation of total effective mass and rest mass of inner and outer floats, for the geometry specified in Appendix A, with the masses considered separately.

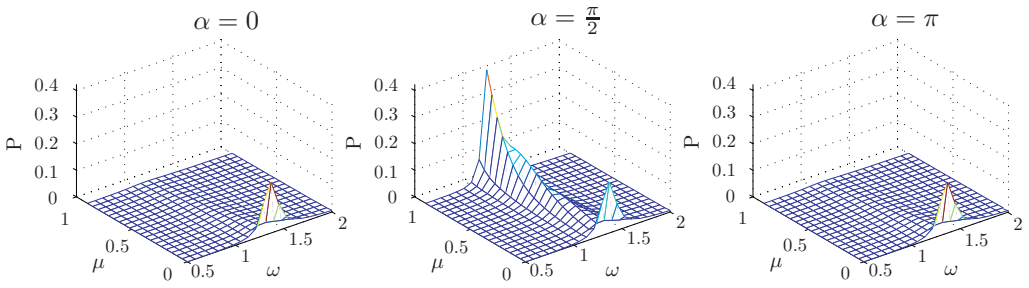

Figure A.14: Plots of non-dimensional power P (cf. (20)) comparing the effect of changing added onset α over a two-parameter space varying μ and ω. Switching onset boundary is optimal ($\beta = \frac{\pi}{2}$), forcing is equivalent on both masses ($f_1 = f_2 = 1$), damping $\delta_2 = 0.05$, momentum coefficient ϵ is 0.8, and the tuning ratio is unity ($\gamma = 1$).

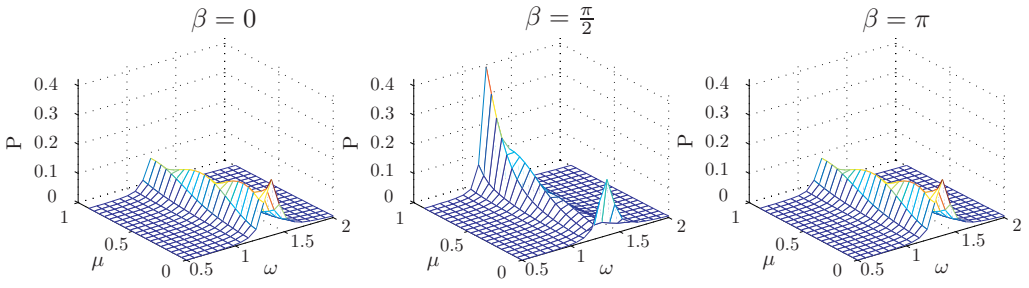

Figure A.15: Plots of non-dimensional power P (cf. (20)) comparing the effect of changing added mass period β over a two-parameter space varying μ and ω. Switching onset boundary is optimal ($\alpha = \frac{\pi}{2}$), forcing is equivalent on both masses ($f_1 = f_2 = 1$), damping $\delta_2 = 0.05$, momentum coefficient ϵ is 0.8, and the tuning ratio is unity ($\gamma = 1$).

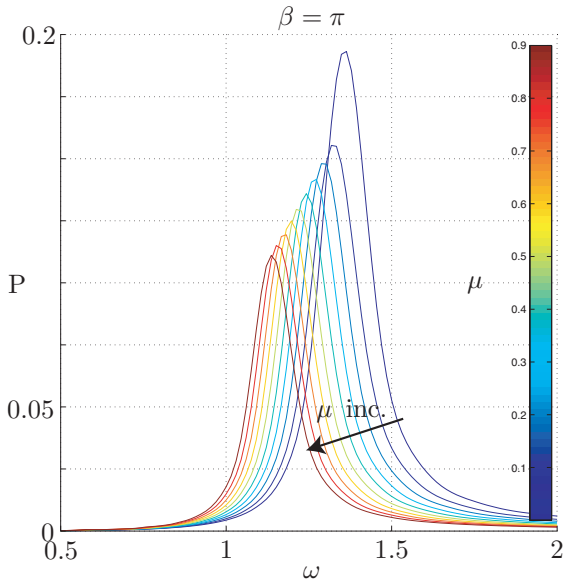

Figure A.16: Resonance peak shift of non-dimensional P (cf. (20)) for the value of $\beta = \pi$ and increasing μ.

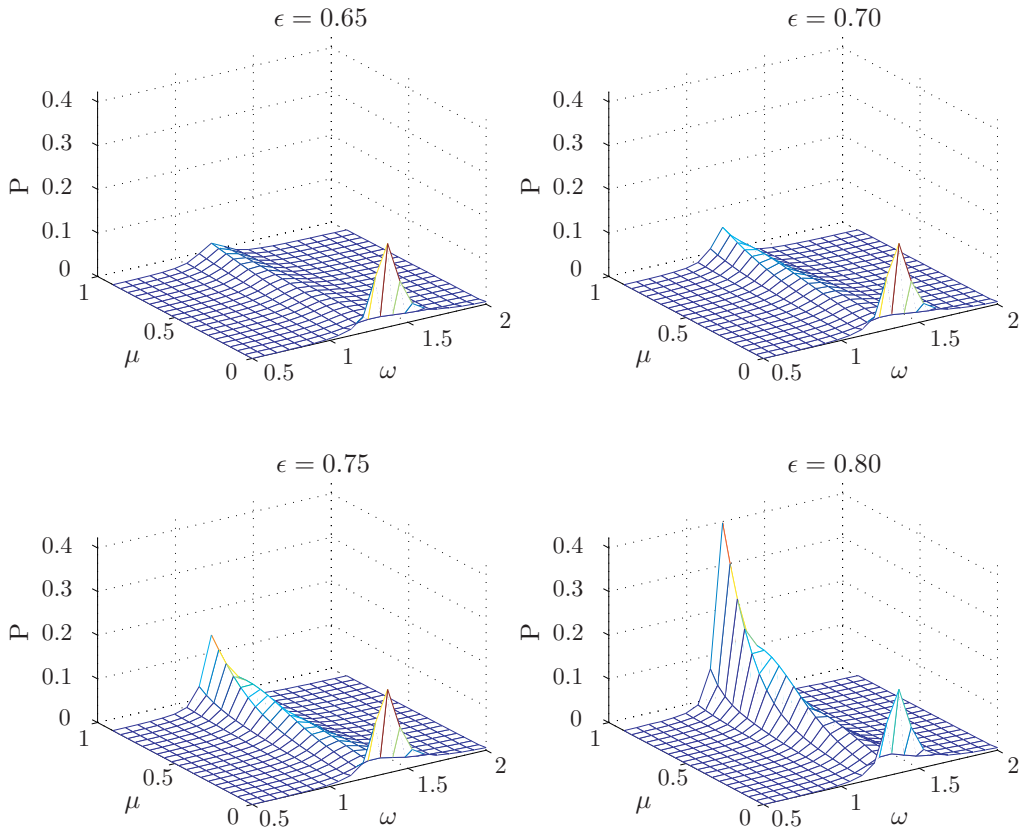

Figure A.17: Plots of non-dimensional power P (cf. (20)) comparing the effect of changing momentum coefficient ϵ over a two-parameter space varying μ and ω. Switching boundaries are optimal ($\alpha = \frac{\pi}{2}$ and $\beta = \frac{\pi}{2}$), forcing is equivalent on both masses ($f_1 = f_2 = 1$), damping $\delta_2 = 0.05$, and the tuning ratio is unity ($\gamma = 1$).

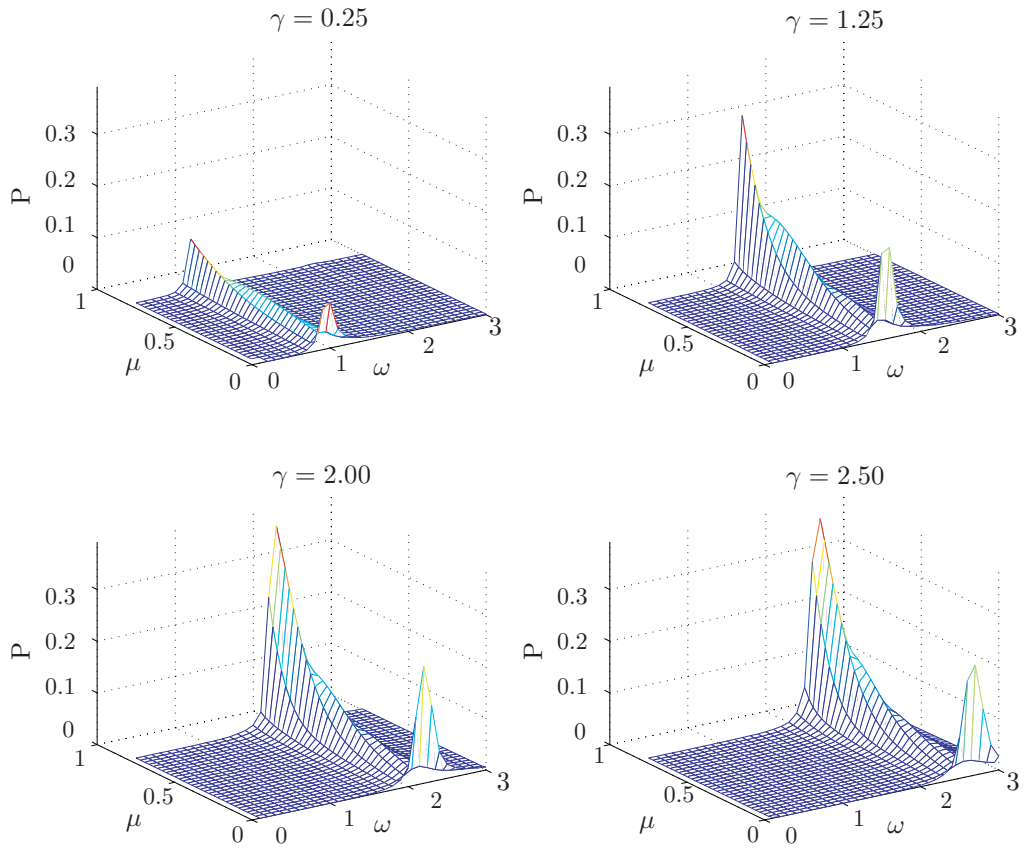

Figure A.18: Plots of non-dimensional power P (cf. (20)) comparing the effect of changing tuning ratio γ over a two-parameter space varying μ and ω. Switching boundaries are optimal ($\alpha = \frac{\pi}{2}$ and $\beta = \frac{\pi}{2}$), forcing is equivalent on both masses ($f_1 = f_2 = 1$), damping $\delta_2 = 0.05$, and the momentum coefficient ϵ is 0.8.

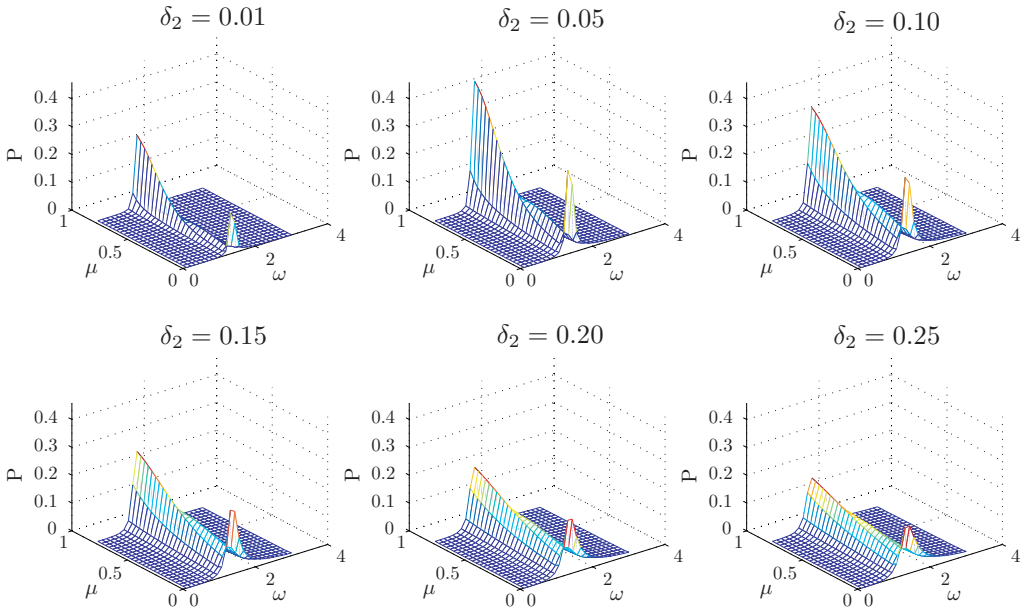

Figure A.19: Plots of non-dimensional power P (cf. (20)) comparing the effect of damping δ_2 over a two-parameter space varying μ and ω. Switching boundaries are optimal ($\alpha = \frac{\pi}{2}$ and $\beta = \frac{\pi}{2}$), forcing is equivalent on both masses ($f_1 = f_2 = 1$), momentum coefficient ϵ is 0.8, and the tuning ratio is unity ($\gamma = 1$).

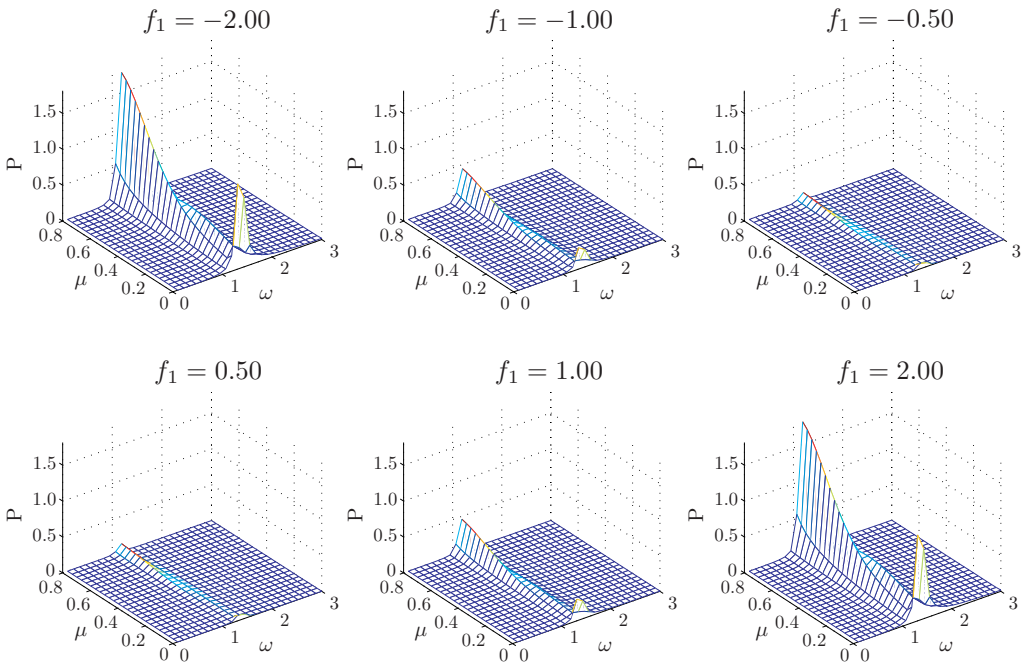

Figure A.20: Plots of non-dimensional power P (cf. (20)) comparing the effect of forcing f_1 over a two-parameter space varying μ and ω. Switching boundaries are optimal ($\alpha = \frac{\pi}{2}$ and $\beta = \frac{\pi}{2}$), forcing on M_2 is equal to 1 ($f_2 = 1$), damping $\delta_2 = 0.05$, momentum coefficient ϵ is 0.8, and the tuning ratio is unity ($\gamma = 1$).

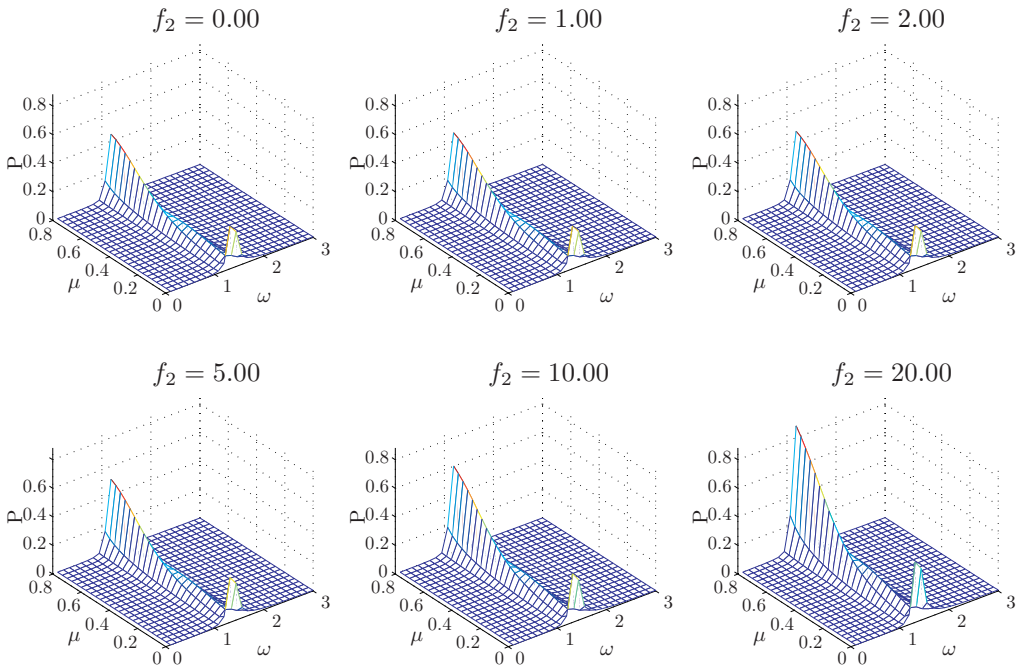

Figure A.21: Plots of non-dimensional power P (cf. (20)) comparing the effect of forcing f_2 over a two-parameter space varying μ and ω. Switching boundaries are optimal ($\alpha = \frac{\pi}{2}$ and $\beta = \frac{\pi}{2}$), forcing on M_1 is equal to 1 ($f_1 = 1$), damping $\delta_2 = 0.05$, momentum coefficient ϵ is 0.8, and the tuning ratio is unity ($\gamma = 1$).

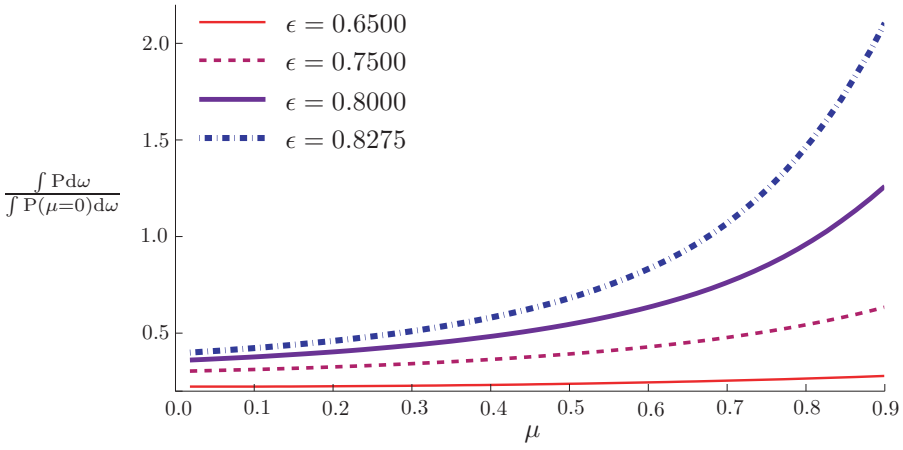

Figure A.22: Relative non-dimensional power harvested with mass modulation normalized to the nominal ($\mu = 0$) case, integrated for $\omega \in [0, 3]$, for a range of values of the momentum coefficient ϵ. Switching boundaries are optimal ($\alpha = \frac{\pi}{2}$ and $\beta = \frac{\pi}{2}$), forcing is equivalent on both masses ($f_1 = f_2 = 1$), damping $\delta_2 = 0.05$, and the tuning ratio is unity ($\gamma = 1$).

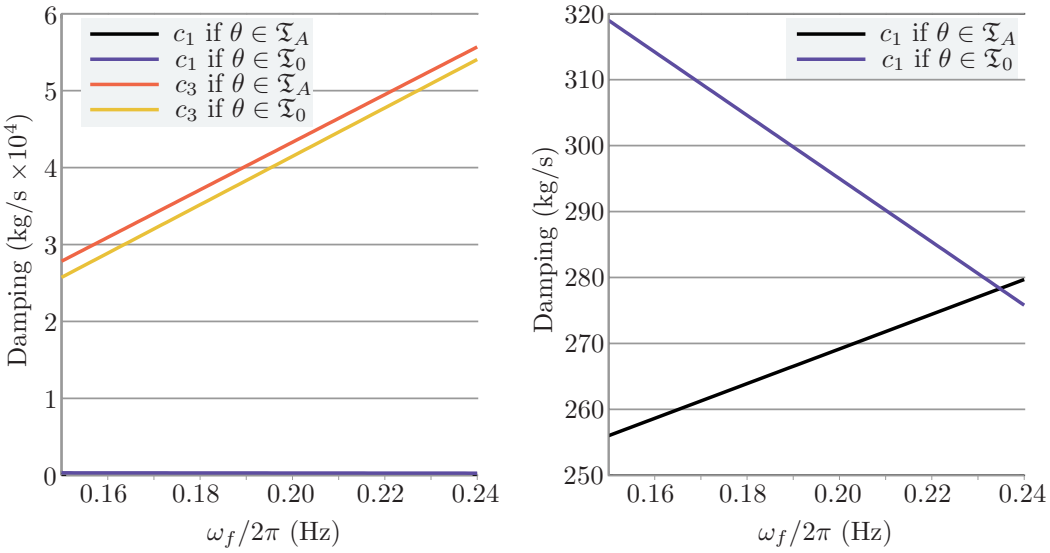

Figure A.23: AQWA simulation damping values.

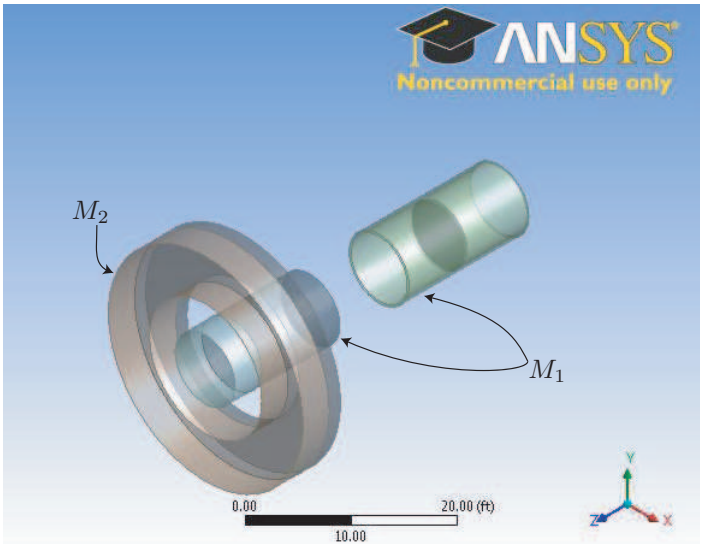

Figure A.24: Hydrodynamic model used to generate system parameters, with M_1 in modulated (M_1^{On}) state.

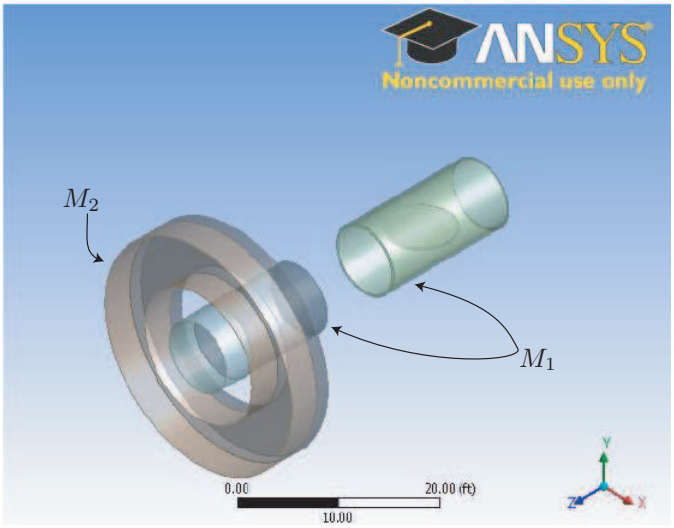

Figure A.25: Hydrodynamic model used to generate system parameters, with M_1 in the unmodulated (M_1^{Off}) state.